Article

Intermittent lab earthquakes in dynamically weakening fault gouge

V. Rubino[1 ✉], N. Lapusta[2,3] & A. J. Rosakis[1]

Large and destructive earthquakes on mature faults in Earth's crust occur as slip in a layer of a fine granular material—fault gouge—produced by comminution during sliding[1,2]. A range of insights into the frictional resistance of faults—one of the main factors controlling earthquake nucleation, dynamic propagation and arrest, and hence the destructive ground shaking of earthquakes[2,3]—has been obtained in experiments with spatially uniform slip imposed in small samples[2,4–21]. However, how various features of gouge friction combine to determine spontaneous progression of earthquakes is difficult to study in the lab owing to substantial challenges with sample sizes and adequate imaging[22]. Here, using lab experiments, we show that spontaneously propagating dynamic ruptures navigate a fault region with fine rock gouge through complex, intermittent slip processes with dramatic friction evolution. These include repeated arrest of rupture propagation caused by friction strengthening at lower slip rates and dynamic earthquake re-nucleation enabled by pronounced rapid friction weakening at higher slip rates consistent with flash heating[8,12,23]. The spontaneous repeated weakening and strengthening of friction in fine rock gouge highlights the fundamental dependence of friction on slip rate and associated processes, such as shear heating, localization and delocalization of shear, and dilation and compaction of the shear layer[6,7,9–21]. Our findings expand experimental support[9,11] of the concept that co-seismic weakening may enable earthquake rupture to break through stable fault regions[24,25], with substantial implications for seismic hazard.

Characterizing the evolution of dynamic slip processes and rock friction during fault slip in Earth's crust is a fundamental step to enhance our understanding of earthquake physics, as friction controls key aspects of earthquakes, including nucleation, shear stress drop and magnitude[2,3], and hence how damaging they can be. How friction evolves is a topic of significant research and debate[2,4–21]. Earthquakes propagate along localized zones in layers of gouge—the fine-grain rock powder present in natural faults that results from wear along the slipping surfaces[1,2]. Laboratory experiments have shown that gouge friction depends on how fast slip accumulates—that is, slip velocity (also known as slip rate)—and its history, as described by standard rate-and-state friction laws at slow, aseismic slip rates of several orders of magnitude around $1\,\mu m\,s^{-1}$ (refs. [4,6]). Velocity-strengthening faults increase their resistance with slip velocity and respond to slow tectonic loading by aseismic slip, whereas velocity-weakening faults allow for runaway frictional instabilities and dynamic earthquake ruptures[2,4,26]. At seismic slip rates of around $1\,m\,s^{-1}$, several additional dynamic weakening mechanisms may play a role, including flash heating, shear melting, thermal pressurization of pore fluids and elastohydrodynamic nanoparticle, or silica gel, lubrication[5,7–16,18,20,23,27].

Most laboratory experiments on static and dynamic rock-gouge friction impose spatially uniform slip with a predetermined slip-rate history in relatively small samples[2,4–21]. Although such experiments are indispensable for identifying key features of gouge friction, they cannot provide insight on how the various features of frictional resistance may combine during spontaneous dynamic rupture propagation, when slip evolves owing to coupling between dynamic stressing—determined by the history of slip everywhere on the interfaces and transmitted by dynamic waves—and dynamically evolving history-dependent friction. Experiments in analogue materials have revealed many features of spontaneous slip accumulation[28–34]; however, they do not consider sliding in rock materials. Some recent experiments have studied earthquake nucleation and slip evolution in large rock samples[22] and analogue samples with rock gouge on the interface[35], but they have not considered spontaneous dynamic rupture propagation over distances several times the nucleation size owing to limitations in sample dimensions and/or other features of the experimental setup. Hence the evolution of spontaneous dynamic rupture on gouge-filled faults has mostly been studied through numerical modelling, which uses laboratory-based but simplified, empirically formulated friction laws[24,25,27].

Here we present laboratory experiments that mimic earthquake sequences in mature faults and show how spontaneous dynamic rupture navigates a fault region with (nominally uniform) rock gouge (Fig. 1). The rupture experiences repeated arrest, dynamic re-nucleation

[1]Graduate Aerospace Laboratories, California Institute of Technology, Pasadena, CA, USA. [2]Mechanical and Civil Engineering, California Institute of Technology, Pasadena, CA, USA. [3]Seismological Laboratory, California Institute of Technology, Pasadena, CA, USA. ✉e-mail: vito.rubino@caltech.edu
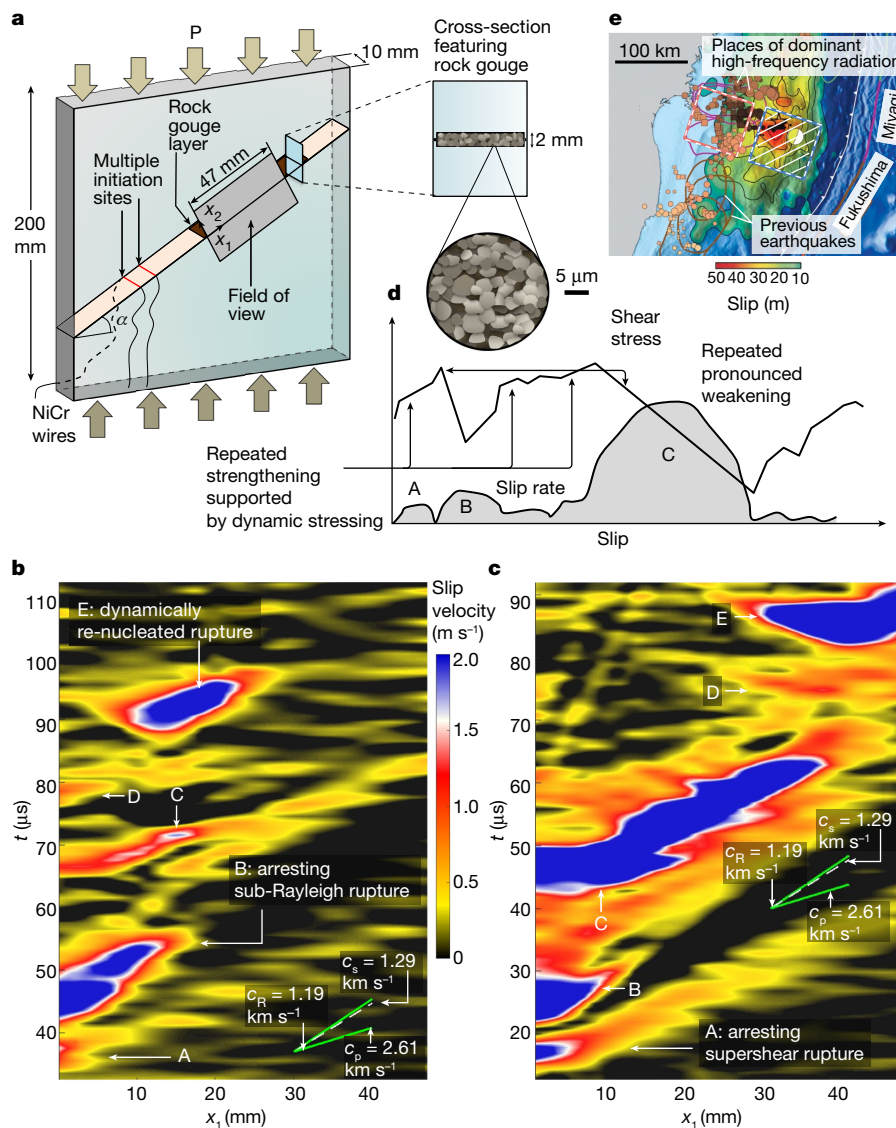
Fig. 1 | Intermittent lab earthquake rupture sequences in rock gouge.
a, Experimental Homalite specimen with a rock-gouge layer that mimics a prestressed fault in the Earth. Two wires (red) are used to initiate two consecutive dynamic ruptures that develop within the Homalite interface before navigating the gouge layer in two distinct rupture sequences. **b**, **c**, Evolution of slip velocity along the gouge interface for the two rupture sequences, featuring repeated rupture propagation arrest and dynamic re-nucleation, with five main dynamic sub-events A–E constituting a highly intermittent but still dynamic rupture of the gouge layer. **d**, Illustration of how

such complex rupture behaviour is enabled by dramatic evolution of shear stress and hence friction, featuring repeated strengthening supported by dynamic stressing followed by pronounced dynamic weakening. **e**, Slip distribution of the 2011 M_w 9.0 Tohoku-Oki earthquake[55], which can be explained by dynamically induced rupture of dynamically weakened shallow fault portions that initially served as a strengthening barrier, similar to the interpretation of our laboratory findings. Panel **e** adapted with permission from ref. [24], Springer Nature Ltd.

and propagation of multiple dynamic events. The complex slip behaviour is accompanied by rapid friction changes that combine repeated sustained strengthening at lower slip rates with dramatic weakening at higher slip rates. Although slower-velocity strengthening and faster-velocity weakening have been studied in previous experiments[2,4–21], mostly separately, their repeated appearance at the same locations along the fault within the same dynamic event and their pronounced combined effect on spontaneous earthquake rupture are quite surprising. The occurrence, detailed visualization and quantification of the multiple resulting dynamic rupture sub-events are possible owing to our highly instrumented laboratory setup that allows for the miniaturization of the dynamic processes by using an analogue bulk material, Homalite, while considering ruptures in rock gouge (next section and Methods).

Creating and capturing lab earthquakes

We produce spontaneously propagating dynamic ruptures and study how they navigate rock-gouge interfaces (Fig. 1 and Extended Data Fig. 1) embedded into our laboratory setup that mimics faults in Earth's crust (Methods). For these experiments, we have developed a hybrid configuration featuring a quartz gouge fault embedded along the interface of a polymeric specimen made of Homalite-100. The hybrid configuration allows us to retain the advantage of producing dynamic ruptures offered by smaller instability length scales owing to bulk Homalite properties[33] while permitting us to study more realistic fault materials (Methods). This important advantage allows us to observe well developed ruptures within a specimen size of tens of centimetres instead of metres, as would be required for bulk rocks[22] (Methods).

We use fine-grained quartz powder, with most particles being 5 μm in diameter or smaller, to simulate the fine gouge found along the principal slipping zones of mature faults[1,23]. Previous versions of this setup featuring dynamic ruptures along Homalite interfaces, without gouge, have been successfully used to investigate a number of fundamental issues in earthquake physics, including the sub-Rayleigh-to-supershear transition, rupture directionality owing to the bimaterial effect and the pulse-like-to-crack-like transition[28,29].

In this study, two rupture sequences are initiated by means of small bursts induced by two wires placed across the fault (Fig. 1a). The initial pre-load level ($P = 14$ MPa) and the fault inclination angle ($\alpha = 29°$) result in the initial fault-resolved shear and normal stresses of 6 MPa and 11 MPa, respectively. After the first sequence of ruptures has propagated and arrested, the prestress is reset to the same level and a new rupture is initiated by triggering another wire (Extended Data Fig. 1 and Methods). Our dynamic imaging captures the complex full-field behaviour of ruptures propagating through the gouge interface (Fig. 1b, c and Supplementary Videos 1–3), including the slip history of dynamic event sequences (Fig. 2a, b) and the friction evolution along the fault (Fig. 2c). These measurements are enabled by our recent advances in quantifying the full-field distributions of displacements, velocities and stresses using our recently developed ultrahigh-speed imaging technique based on the digital image correlation (DIC) method[33,36–38].

Intermittent dynamic rupture in gouge

We find that slip in the rock gouge proceeds through sequences of dynamic, laboratory earthquake events triggered by dynamic rupture nearby. The first sequence of events within our observation window starts with a supershear rupture entering the gouge layer and arresting shortly after (rupture A in Figs. 1b, 2a, Extended Data Figs. 2, 3 and Supplementary Video 1), which indicates that the gouge layer initially acts as a barrier to the propagating dynamic rupture. As the rupture arrests, it leaves residual, much smaller, ongoing slip (with slip rates at the resolution limit of 0.4 m s^{-1}, see Methods; Fig. 1b). At the same time, it is clear that slip continues outside the observation window, along the Homalite interface, as the arrest of rupture upon reaching a barrier can be only gradual, with the healing fronts propagating at best with the wave speeds[39,40]. As a manifestation of that, the next attempt to rupture the gouge layer comes from the trailing-Rayleigh rupture feature (event B in Figs. 1b, 2a), which typically follows the supershear rupture tip (Extended Data Fig. 2a)[37]. This rupture also loses steam shortly after entering rock gouge, with the gouge again acting as a barrier to the advancing rupture. Again, heterogeneous slower slip is left in its wake. The ongoing slip on the Homalite interface results in other accelerated slip events at the edge of the gouge, such as events C and D in Figs. 1b, 2a.

Next, in a departure from these attempts of slip to penetrate into the gouge from the edge, a prominent dynamic rupture E accelerates from within the gouge (at 87.6 μs; Figs. 1b, 2a, Extended Data Fig. 4 and Supplementary Video 1). This laboratory rupture initially grows bilaterally, then propagates into the gouge, and finally arrests well within the imaged window. For dynamic rupture E to initiate within the gouge, despite prior rupture arrest there and in a short time (microseconds), it clearly requires either rapid additional loading through dynamic wave-mediated stress changes, or rapid dynamic weakening, or both. In that sense, event E and other similar events are dynamically triggered. Event E starts in the general location where prior ruptures B and C partially arrest (Figs. 1, 3), indicating the importance of stress concentrations there owing to the (dynamic) process of establishing the static stress field[40] corresponding to the already accumulated slip in events B–D (Extended Data Figs. 3, 4, 9). At the same time, event E nucleates around $x_1 \approx 12$ mm (where x_1 is parallel to the interface and indicates the distance from the left boundary of the imaging window; see Fig. 1a), not at the largest stress concentration left by the prior arrests (which is

at $x_1 = 18$–20 mm; Extended Data Fig. 9), and the nucleation process of event E occurs over dynamic timescales, suggesting that the dynamic re-nucleation is promoted, at least in part, by wave-mediated stress changes. The ongoing slower slip after the partial arrest of event D may also lead to localization processes that can activate weakening mechanisms, for example, owing to flash heating[12,16,33], and our quantification of the fault friction indeed indicates that, as discussed in the next section (Fig. 4).

The second rupture sequence features an initially similar succession of events, with the supershear and sub-Rayleigh portions of the incoming rupture (labelled as ruptures A and B in Fig. 1c) stopping their propagation shortly after entering the gouge layer (Fig. 1c and Supplementary Video 2). However, unlike in the first sequence, seismic slip continues next to the edge of the gouge region with slip rates of about 1 m s^{-1} (Fig. 1c and Extended Data Fig. 5), presumably sustained by continuous dynamic loading by stress waves from the slipping Homalite interface nearby. Eventually, the slip accelerates, leading to event C that propagates into the gouge (Figs. 1c, 2b, 3a–d and Extended Data Fig. 5). The slip-rate profiles along the interface capture the slip acceleration of rupture C and its further propagation (Fig. 3a, dashed and solid blue curves), which arrests within the gouge.

Next, in a new development, dynamic rupture enters the field of view from the other end of the observation window at about 73.8 μs (event D in Fig. 1c, 2b, d and Extended Data Fig. 6) and spreads against the main propagation direction of the other ruptures (Fig. 2d, Supplementary Video 2), with the propagation arresting at about 76.8 μs. Although slip in this event is relatively small, its appearance is notable: it clearly indicates rupture initiation to the right of the observation window, whereas some of the gouge interface within the window still has not experienced any significant slip. This supports the role of dynamic stress changes in triggering the event at a (nearby) distance. Shortly thereafter (at about 81.8 μs), slip dynamically accelerates within the portion of the interface where event C has arrested and which has been ruptured by event D, and spreads as dynamic rupture E (Figs. 2b, 3a, e, f and Extended Data Fig. 6).

In each sequence, rupture events A–E can be (and observationally would be) considered the same dynamic event that stops propagating multiple times but always maintains seismic slip rates of 0.4–1 m s^{-1}, accelerating and re-initiating dynamic propagation owing to dynamic stress waves. In the second sequence, events A–E take about 70 μs overall to cross the gouge region of 47 mm, from the beginning of event B to when event E exits the field of view. Although the actual local rupture speed is clearly intermittent, the average speed of slip crossing the gouge layer is about 0.7 km s^{-1} or 0.5 of the bulk shear-wave speed, clearly indicating that the whole process is quite dynamic.

Considering the local rupture speeds leads to an additional insight that the dynamically re-nucleated events initiate inside the 10-mm-thick interface and then propagate to the lateral free surface where we observe them by DIC (Extended Data Fig. 7 and Methods). This insight indicates that the (dynamic) nucleation sizes are smaller, and potentially much smaller, than the interface width of 10 mm. The nucleation size typically scales with the shear modulus of the bulk material, which is about 20 times larger for rocks than for Homalite, and inversely scales with the effective normal stress, which is $\sigma_0 = 11$ MPa in this case (Methods). Hence the corresponding dynamic nucleation size for a case of rock gouge within rock bulk at 11 MPa effective normal stress would be less than (and potentially much less than) 10 mm × 20 = 0.2 m. This upper bound is notably smaller than quasi-static nucleation sizes (1 m at $\sigma_0 = 6$ MPa, translating into 0.57 m at $\sigma_0 = 11$ MPa) observed in rock experiments in large samples[22] (Methods), with the caveat that the friction properties may also be different between the two experiments. This comparison suggests that dynamic nucleation sizes may be much smaller than quasi-static ones, consistent with other studies[34], numerical simulations[41] and our experiments on rupture triggering by fluid injection[42].
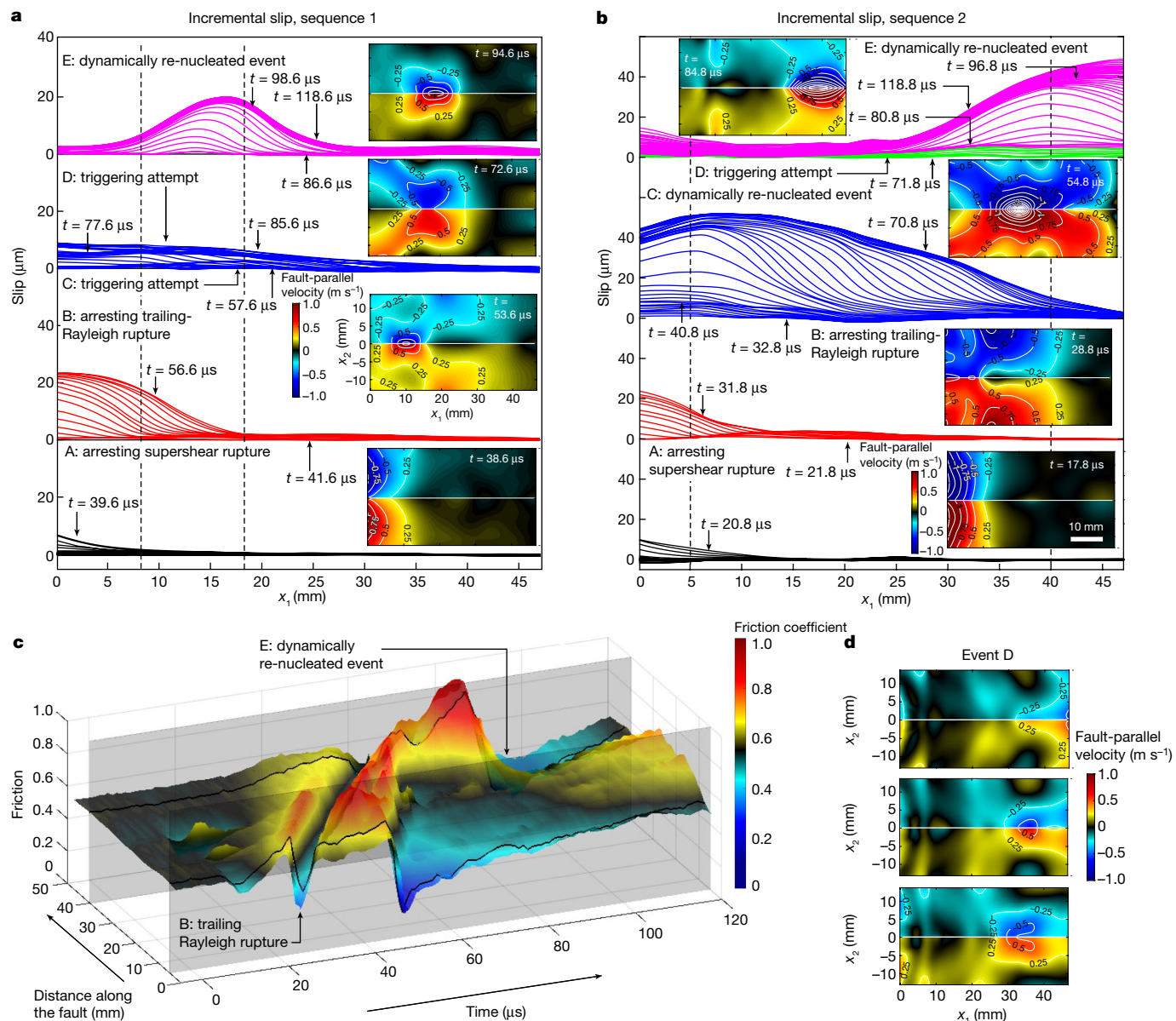
Fig. 2 | Slip history for the two rupture sequences. a, b, Incremental slip versus position along the interface illustrating, from bottom to top, the five main events A–E in rupture sequences 1 (**a**) and 2 (**b**). Events E dynamically nucleate well within the gouge region. Colours separate the slip accumulation history into four periods, with the same colours used in Figs. 3, 4. Insets: the full field fault-parallel particle velocity at selected time frames. The vertical black lines indicate the locations of friction versus slip evolution given in Fig. 4. **c,** Friction evolution with time and distance along the interface. Two planes, at $x_1 = 5$ mm and $x_1 = 40$ mm, intersect the friction surface and provide the friction time history at those two locations. **d,** Snapshots of the fault-parallel particle velocity during event D of the second rupture sequence.

Dramatic friction changes in gouge

The highly intermittent rupture propagation within the gouge corresponds to marked variations of the friction coefficient, obtained as the ratio of shear and normal stresses (Fig. 4 and Extended Data Figs. 8, 9). During the first sequence, friction shows a purely strengthening behaviour with the arrival of the first supershear rupture, increasing by $\Delta f \approx 0.1$, over about 5 μm of slip in some locations (Extended Data Fig. 10). During the second sequence, the behaviour is similar. When the trailing-sub-Rayleigh ruptures arrive, friction drops substantially, by $\Delta f \approx 0.22$ and $\Delta f \approx 0.35$ for the first and second sequences, respectively, again over only 5 μm or so of slip (Fig. 4a, e). Similarly striking dynamic friction strengthening and weakening are exhibited during rupture events C and D dynamically re-nucleating within the gouge interface. For example, before and at the beginning of event C of the

second sequence (Fig. 2b), a representative location ($x_1 = 5$ mm) shows sustained strengthening of $\Delta f \approx 0.1$, this time over about 15 μm of slip (from about 18 μm to about 33 μm of slip), followed by dramatic weakening during event C of $\Delta f \approx 0.58$ over only about 30 μm of slip, down to $f = 0.15$. The subsequent event E shows even more marked strengthening followed by an even more prominent weakening, with the decrease of the friction coefficient by $\Delta f \approx 0.64$ (Fig. 4f, h). All pronounced weakening episodes are followed by pronounced healing, with $\Delta f \approx 0.58$ and $\Delta f \approx 0.27$ for ruptures C and E, respectively (Fig. 4e, f). It is noted that healing occurs extremely rapidly, over several microseconds in time and several micrometres in slip.

The substantial strengthening of the interface—which precedes the fastest sliding episodes—generally occurs with increasing slip rates, and hence it is conceptually similar to velocity strengthening of the standard rate-and-state friction laws[4,6], although it appears to
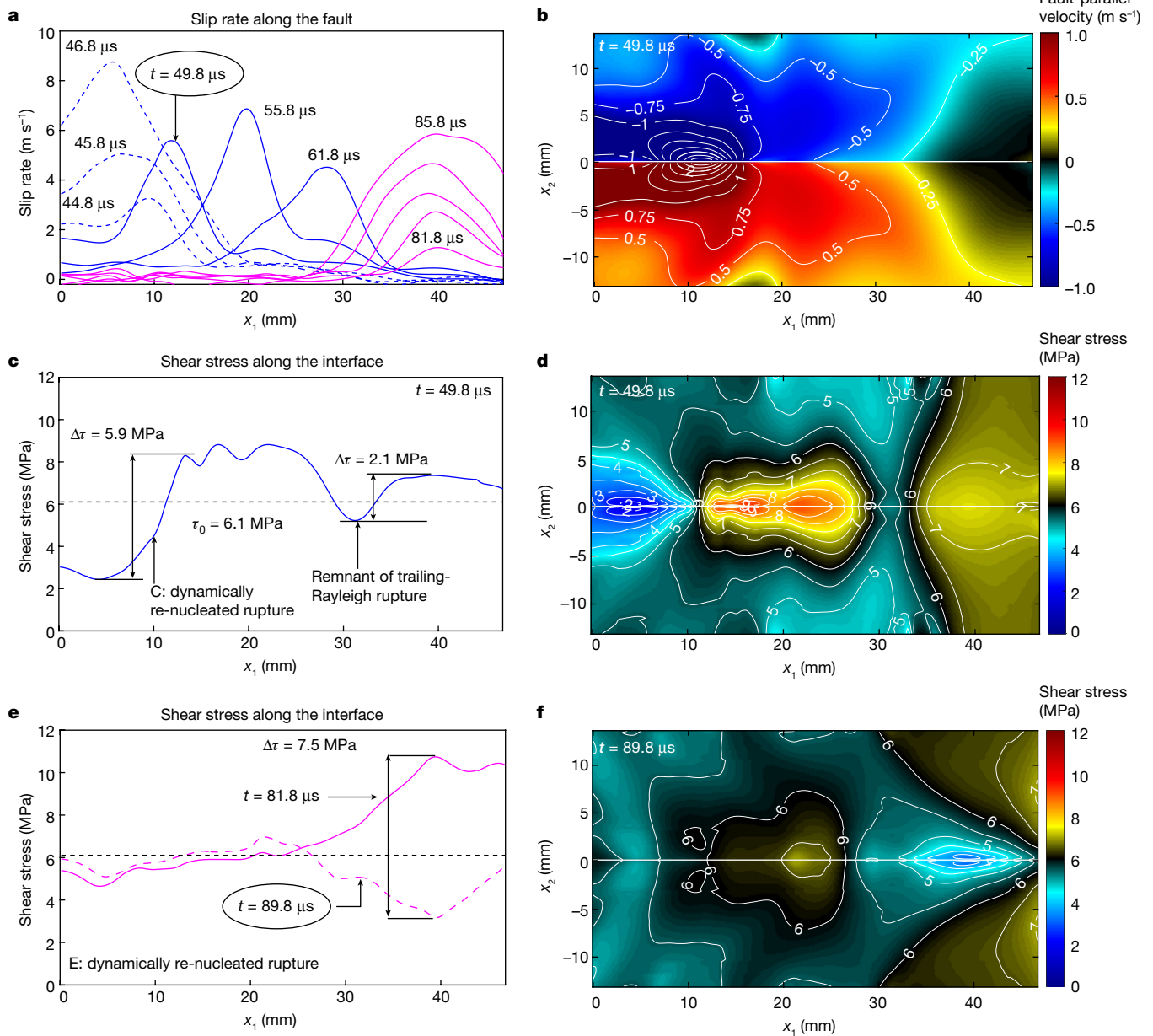
Fig. 3 | Evolution and characteristics of the two sub-events in the second rupture sequence. a, Slip rate along the fault for several time instances revealing the initiation and propagation (dashed and solid blue lines) of rupture C and progression (purple lines) of rupture E. **b**–**d**, Full-field distribution of the fault-parallel particle velocity (**b**), shear stress along the interface (**c**) and full-field map of the shear stress at a selected time (**d**), highlighting propagation of event C. **e**, **f**, Distribution of shear stress along the interface before and after event E (**e**) and full-field map of the shear stress after event E (**f**).

be quantitatively different. For example, as slip rates increase from about $V_1 = 1$ m s^{-1} to about $V_2 = 2$ m s^{-1} (over about 15 μm of slip) before event C (Fig. 4g), friction increases by about 0.1 (Fig. 4e), which is much larger than about $0.01\ln(V_2/V_1) = 0.007$ expected from the standard rate-and-state friction formulations and parameters (Methods). It is noted that the observed friction increase cannot be explained by the rate-and-state direct effect of steady-state velocity-weakening friction, as strengthening owing to the direct effect occurs with negligible slip compared with subsequent weakening, as observed in numerical models[43] and dynamic ruptures in Homalite interfaces[33]. In contrast, the rock gouge in our experiments experiences sustained strengthening over slip scales that are comparable to those of weakening (Figs. 1d, 4, Extended Data Fig. 10 and Methods). It is also noted that the rupture arrest in rock gouge cannot be easily interpreted in terms of higher

values of fracture (also known as breakdown) energy, a concept widely used to describe the interface resistance to fracture which, in some cases, can be analogous to frictional failure[2,3,31,44,45]. This is because the small-scale yielding approximation—that makes the fracture (breakdown) energy a governing parameter in crack propagation—does not apply to the gouge resistance we measure, which 'yields' and 'unyields' repeatedly and weakens to different levels as slip accumulates.

The observed pronounced weakening and healing also cannot be solely due to the relatively mild logarithmic friction variations described by standard rate-and-state laws. Instead, our measurements of rapid friction weakening are consistent with the flash-heating weakening mechanism[8,12,23]. During flash heating, the micrometre-scale tips of contacting asperities heat and weaken for large enough slip rates, resulting in a marked drop in frictional strength with a pronounced
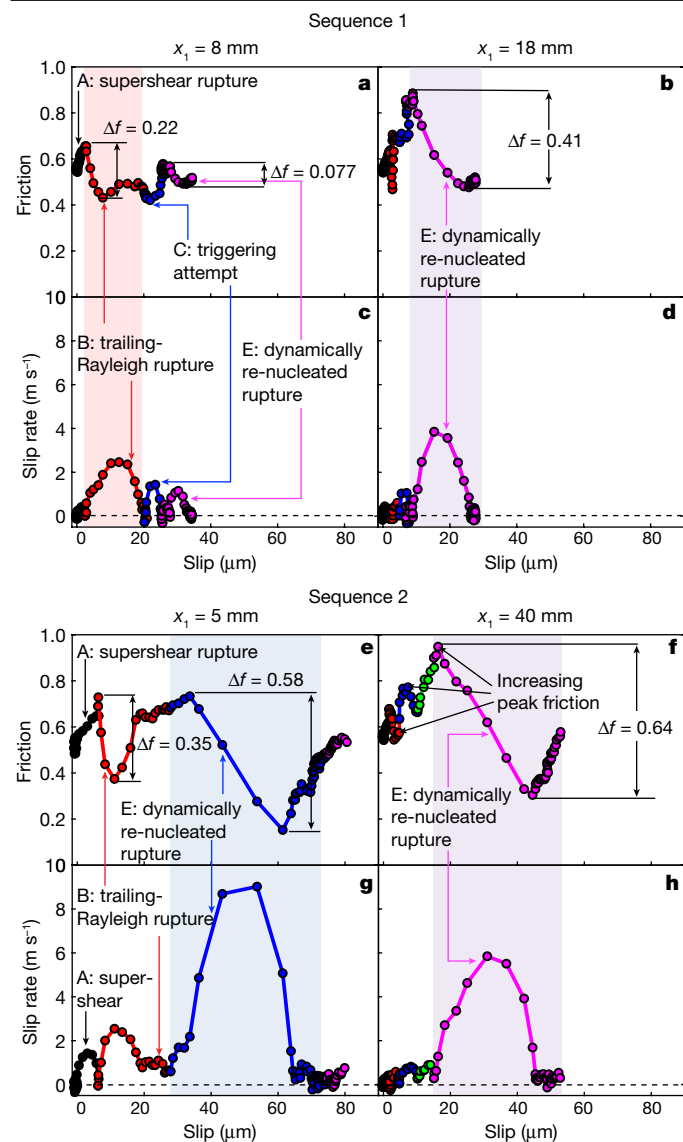
Fig. 4 | Evolution of dynamic friction within the rock gouge with repeated strengthening, pronounced weakening and healing. a–h, Friction versus slip (**a, b, e, f**) and slip rate versus slip (**c, d, g, h**) for the rupture sequences 1 (**a–d**) and 2 (**e–h**), for selected locations along the interface. The friction evolution in both sequences is characterized by marked strengthening, for slip rates as high as 0.5–2 m s⁻¹, followed by dramatic weakening at higher slip rates consistent with flash heating. It is noted that strengthening and weakening occur over comparable slip scales of 5–30 μm (see also Extended Data Fig. 10) and, together, explain the intermittent rupture arrest and re-nucleation.

$1/V$ dependence on the slip velocity V. Owing to the highly local and transient nature of the process, frictional strength is quickly recovered when the slip rate subsides. The lowest values of the friction coefficient we find, 0.15–0.2, are consistent with previous measurements of flash-heating weakening in quartz gouge[12]. These very low friction values also confirm that we have slip within the quartz gouge, and not on the gouge–Homalite interface, as the lowest dynamic friction on Homalite interface is 0.26, even for much higher slip rates[33]. It is noted that dynamic weakening in our experiments occurs over short slip scales of the order of 5–30 μm, consistent with the theories of flash heating[23]. The pronounced weakening occurs for slip rates larger than 0.5–2 m s⁻¹, consistent with previous measurements on rock gouge[14,16] and notably larger than weakening slip rates of the order of 0.1 m s⁻¹ for initially bare rock surfaces[12,16].

Although our dynamic friction measurements are consistent with the theory and previous quantification of flash heating, several other dynamic weakening mechanisms have been proposed and could contribute to the weakening we observe—as well as to weakening on natural faults with comparable consequences—including shear melting, silica gel lubrication, and amorphous nanopowder and nanoparticle lubrication[5,7,13,15,20]. Other weakening mechanisms commonly used to explain fault weakening are thermal pressurization of pore fluids[23] and elastohydrodynamic lubrication of faults[3] but these mechanism cannot be operating here as they require the presence of fluids and our experiments are performed on dry gouge.

Implications for earthquake processes

To summarize, our laboratory earthquake sequences navigate a fault region filled with rock gouge through intermittent rupture propagation that exhibits rupture arrest, dynamic stressing and dynamic re-nucleation in triggered events, all within timescales comparable to a single dynamic rupture. The gouge-filled interface initially behaves as a barrier, stopping rupture propagation, consistent with strengthening friction at slip velocities at and below 0.5–2 m s⁻¹. However, as dynamic stressing of the arrest locations leads to higher slip velocities, dynamic weakening consistent with flash heating is activated, leading to dynamic re-nucleation of rupture propagation. Overall, these faster and slower slip events appear as a cascade, similar to the observations of earthquake triggering by cascade of foreshocks[46,47].

We find dramatic repeated variations of friction in the rock gouge, with substantial sustained strengthening at lower slip rates of 0.5–2 m s⁻¹, followed by rapid dynamic weakening at higher slip rates that enable the fault to lose 50–75% of its strength in just tens of micrometres of slip, and then followed by equally rapid healing in several tens of microseconds. These pronounced repeated changes, not only in the values of friction but also in its nature—from substantially strengthening to rapidly weakening and back—explain the intermittent rupture propagation. The friction evolution we observe is conceptually consistent with a combination of velocity-strengthening friction at lower slip rates and pronounced dynamic weakening at higher slip rates.

Our friction measurements stand in contrast to a common assumption that friction generally weakens once during dynamic events, as captured by slip-weakening friction formulations with peak friction at (or close to) the onset of seismic slip evolving to lower dynamic friction[2,3,44]. The rupture behaviour observed in our experiments can only be reproduced if the fundamental dependence of friction on slip velocity, in addition to other state variables, is properly accounted for; it cannot be replaced by an 'effective' slip-weakening friction.

Our experiments reveal that complex spontaneous sequences of dynamic events can occur even on nominally homogeneous—and homogeneously prestressed—gouge interfaces, simply owing to the complex local dependence of friction on slip velocity and its history. This is in contrast to our previous studies on Homalite interfaces, which have documented accelerating continuous ruptures under similar loading conditions[33,37]. The main difference is the unexpectedly pronounced, sustained and repeated strengthening of the rock gouge even at already seismic slip rates of 0.5–2 m s⁻¹ and even after repeated pronounced weakening at higher slip rates. This repeated strengthening is unexpected given previous findings of more long-lived evolution from strengthening to weakening with slip[19] and highlights the challenge of understanding friction evolution in granular layers, which can accommodate slip with different levels of evolving localization and delocalization of the shear and exhibit grain-size dependence, in addition to other effects[2,4–21].

The repeated dynamic re-nucleation of rupture propagation in our experimental fault gouge is reminiscent of near-field dynamic triggering[48,49], and suggests that enhanced dynamic weakening may have a role in dynamic triggering. An increasing body of evidence indicates

that earthquakes can be triggered by dynamic stress changes[48–51]. Our experiments provide evidence of dynamic re-nucleation occurring on the same timescales as the dynamic stress perturbations, although the process occurs within the fault area of stress concentration caused by arrest of prior events. Seismic events dynamically triggered in nature are also thought to occur in special places, such as locations of high prestress or low strength[49–51]. Our findings indicate that rapid dynamic strength evolution may also have a role. An important issue with dynamic triggering is how to sufficiently speed up the slow nucleation process so that it can occur within the time of dynamic stress perturbations, which are relatively short. For example, with standard rate-and-state friction laws, dynamic waves can only trigger nucleating sites that would rupture very soon anyway[52]. Our experiments suggest that enhanced dynamic weakening may provide an important additional ingredient: if the short-lived dynamic stressing by waves raises the slip rates enough to activate enhanced dynamic weakening, either owing to flash heating or by other numerous mechanisms proposed that may require lower slip rates[5,7,8,10–16,18,20,23,27], then the nucleation can potentially be achieved on dynamic timescales and from a much smaller spatial extent, as observed in our experiments and supported by other studies[34,41,42].

Our experiments show that pronounced dynamic weakening in fine fault gouge can occur with very small amounts of dynamic slip, 5–30 μm. This finding suggests that dynamic weakening may contribute to slip processes in earthquakes of all sizes, including microseismicity, which may explain the high stress drops and other observations for some microseismic events[53]. It is noted that the amounts of dynamic slip needed for pronounced dynamic weakening in fine fault gouge are much smaller than slips of the order of 1–10 mm needed for transition from velocity-strengthening to moderately velocity-weakening friction in slow-friction sliding experiments[6,19].

Finally, our experiments illustrate how dynamic rupture may navigate initially velocity-strengthening fault regions, which, in general, present a barrier to dynamic rupture propagation. Despite the pronounced dynamic weakening, our laboratory ruptures still lose steam and nearly arrest, with the gouge layer serving as a strengthening barrier until dynamic weakening is activated. These findings offer additional experimental support[9,11] to the hypothesis that dynamic weakening mechanisms may occasionally allow earthquake ruptures to propagate through stable, creeping fault regions that are at present largely considered immune to seismic slip, with important implications for seismic hazard. Allowing for such propagation explains many short- and long-term observations from the area of the great 2011 moment magnitude (M_w) 9.0 Tohoku earthquake[24] (Fig. 1e) as well as seismic quiescence of several segments of the San Andreas Fault[25]. At the same time, many earthquakes fully arrest in creeping fault regions[54]. Our findings motivate further studies of shear resistance of fault zones to rapid slip rates, both strengthening and weakening, to enable physics-based predictive modelling and seismic hazard assessment.

Online content

Any methods, additional references, Nature Research reporting summaries, source data, extended data, supplementary information, acknowledgements, peer review information; details of author contributions and competing interests; and statements of data and code availability are available at https://doi.org/10.1038/s41586-022-04749-3.

1. Chester, F. M. & Chester, J. S. Ultracataclasite structure and friction processes of the Punchbowl Fault, San Andreas system, California. *Tectonophysics* **295**, 199–221 (1998).
2. Scholz, C. H. *The Mechanics of Earthquakes and Faulting* (Cambridge Univ. Press, 2019).
3. Kanamori, H. & Brodsky, E. E. The physics of earthquakes. *Rep. Prog. Phys.* **67**, 1429–1496 (2004).
4. Dieterich, J. H. in *Treatise on Geophysics* Vol. 4 (ed. Schubert, G.) 93–110 (Elsevier, 2007).
5. Tsutsumi, A. & Shimamoto, T. High-velocity frictional properties of gabbro. *Geophys. Res. Lett.* **24**, 699–702 (1997).
6. Marone, C. Laboratory-derived friction laws and their application to seismic faulting. *Annu. Rev. Earth Planet. Sci.* **26**, 643–696 (1998).
7. Di Toro, G., Goldsby, D. L. & Tullis, T. E. Friction falls towards zero in quartz rock as slip velocity approaches seismic rates. *Nature* **427**, 436–439 (2004).
8. Beeler, N. M., Tullis, T. E. & Goldsby, D. L. Constitutive relationships and physical basis of fault strength due to flash heating. *J. Geophys. Res. Solid Earth* **113**, B01401 (2008).
9. Tanikawa, W. & Shimamoto, T. Frictional and transport properties of the Chelungpu Fault from shallow borehole data and their correlation with seismic behavior during the 1999 Chi-Chi earthquake. *J. Geophys. Res. Solid Earth* **114**, B01402 (2009).
10. Reches, Z. E. & Lockner, D. A. Fault weakening and earthquake instability by powder lubrication. *Nature* **467**, 452–455 (2010).
11. Faulkner, D., Mitchell, T., Behnsen, J., Hirose, T. & Shimamoto, T. Stuck in the mud? Earthquake nucleation and propagation through accretionary forearcs. *Geophys. Res. Lett.* **38**, L18303 (2011).
12. Goldsby, D. L. & Tullis, T. E. Flash heating leads to low frictional strength of crustal rocks at earthquake slip rates. *Science* **334**, 216–218 (2011).
13. Di Toro, G. et al. Fault lubrication during earthquakes. *Nature* **471**, 494–498 (2011).
14. Kitajima, H., Chester, F. M. & Chester, J. S. Dynamic weakening of gouge layers in high-speed shear experiments: assessment of temperature-dependent friction, thermal pressurization, and flash heating. *J. Geophys. Res. Solid Earth* **116**, B08309 (2011).
15. Brown, K. M. & Fialko, Y. 'Melt welt' mechanism of extreme weakening of gabbro at seismic slip rates. *Nature* **488**, 638–641 (2012).
16. Proctor, B. & Di Toro, G. Dynamic weakening of serpentinite gouges and bare surfaces at seismic slip rates. *J. Geophys. Res. Solid Earth* **119**, 8107–8131 (2014).
17. Verberne, B. et al. Frictional properties and microstructure of calcite-rich fault gouges sheared at sub-seismic sliding velocities. *Pure Appl. Geophys.* **171**, 2617–2640 (2014).
18. Boulton, C. et al. High-velocity frictional properties of Alpine Fault rocks: mechanical data, microstructural analysis, and implications for rupture propagation. *J. Struct. Geol.* **97**, 71–92 (2017).
19. Scuderi, M., Collettini, C., Viti, C., Tinti, E. & Marone, C. Evolution of shear fabric in granular fault gouge from stable sliding to stick slip and implications for fault slip mode. *Geology* **45**, 731–734 (2017).
20. Rowe, C. D. et al. Earthquake lubrication and healing explained by amorphous nanosilica. *Nat. Commun.* **10**, 320 (2019).
21. Bedford, J. D., Faulkner, D. R. & Lapusta, N. Fault rock heterogeneity can produce fault weakness and reduce fault stability. *Nat. Commun.* **13**, 326 (2022).
22. McLaskey, G. C., Kilgore, B. D., Lockner, D. A. & Beeler, N. M. Laboratory generated M -6 earthquakes. *Pure Appl. Geophys.* **171**, 2601–2615 (2014).
23. Rice, J. R. Heating and weakening of faults during earthquake slip. *J. Geophys. Res. Solid Earth* **111**, B05311 (2006).
24. Noda, H. & Lapusta, N. Stable creeping fault segments can become destructive as a result of dynamic weakening. *Nature* **493**, 518–521 (2013).
25. Jiang, J. & Lapusta, N. Deeper penetration of large earthquakes on seismically quiescent faults. *Science* **352**, 1293–1297 (2016).
26. Rice, J. R. & Ruina, A. L. Stability of steady frictional slipping. *J. Appl. Mech.* **50**, 343–349 (1983).
27. Noda, H., Dunham, E. M. & Rice, J. R. Earthquake ruptures with thermal weakening and the operation of major faults at low overall stress levels. *J. Geophys. Res. Solid Earth* **114**, B07302 (2009).
28. Xia, K., Rosakis, A. J. & Kanamori, H. Laboratory earthquakes: the sub-Rayleigh-to-supershear rupture transition. *Science* **303**, 1859–1861 (2004).
29. Lu, X., Lapusta, N. & Rosakis, A. J. Pulse-like and crack-like ruptures in experiments mimicking crustal earthquakes. *Proc. Natl Acad. Sci. USA* **104**, 18931–18936 (2007).
30. Ben-David, O., Rubinstein, S. M. & Fineberg, J. Slip-stick and the evolution of frictional strength. *Nature* **463**, 76–79 (2010).
31. Svetlizky, I. & Fineberg, J. Classical shear cracks drive the onset of dry frictional motion. *Nature* **509**, 205–208 (2014).
32. Svetlizky, I. et al. Properties of the shear stress peak radiated ahead of rapidly accelerating rupture fronts that mediate frictional slip. *Proc. Natl Acad. Sci. USA* **113**, 542–547 (2016).
33. Rubino, V., Rosakis, A. & Lapusta, N. Understanding dynamic friction through spontaneously evolving laboratory earthquakes. *Nat. Commun.* **8**, 15991 (2017).
34. Guérin-Marthe, S., Nielsen, S., Bird, R., Giani, S. & Di Toro, G. Earthquake nucleation size: evidence of loading rate dependence in laboratory faults. *J. Geophys. Res. Solid Earth* **124**, 689–708 (2019).
35. Buijze, L., Guo, Y., Niemeijer, A., Ma, S. & Spiers, C. Nucleation of stick-slip instability within a large-scale experimental fault: effects of stress heterogeneities due to loading and gouge layer compaction. *J. Geophys. Res. Solid Earth* **125**, e2019JB018429 (2020).
36. Rubino, V., Rosakis, A. & Lapusta, N. Full-field ultrahigh-speed quantification of dynamic shear ruptures using digital image correlation. *Exp. Mech.* **59**, 551–582 (2019).
37. Rubino, V., Rosakis, A. & Lapusta, N. Spatiotemporal properties of sub-Rayleigh and supershear ruptures inferred from full-field dynamic imaging of laboratory experiments. *J. Geophys. Res. Solid Earth* **125**, e2019JB018922 (2020).
38. Tal, Y., Rubino, V., Rosakis, A. J. & Lapusta, N. Illuminating the physics of dynamic friction through laboratory earthquakes on thrust faults. *Proc. Natl Acad. Sci. USA* **117**, 21095–21100 (2020).
39. Madariaga, R. Dynamics of an expanding circular fault. *Bull. Seismol. Soc. Am.* **66**, 639–666 (1976).
40. Fossum, A. & Freund, L. Nonuniformly moving shear crack model of a shallow focus earthquake mechanism. *J. Geophys. Res.* **80**, 3343–3347 (1975).
41. Kaneko, Y. & Lapusta, N. Variability of earthquake nucleation in continuum models of rate-and-state faults and implications for aftershock rates. *J. Geophys. Res. Solid Earth* **113**, B12312 (2008).
42. Gori, M., Rubino, V., Rosakis, A. & Lapusta, N. Dynamic rupture initiation and propagation in a fluid-injection laboratory setup with diagnostics across multiple temporal scales. *Proc. Natl Acad. Sci. USA* **118**, e2023433118 (2021).

Article

43. Perry, S. M., Lambert, V. & Lapusta, N. Nearly magnitude-invariant stress drops in simulated crack-like earthquake sequences on rate-and-state faults with thermal pressurization of pore fluids. *J. Geophys. Res. Solid Earth* **125**, e2019JB018597 (2020).
44. Palmer, A. C. & Rice, J. The growth of slip surfaces in the progressive failure of over-consolidated clay. *Proc. R. Soc. A* **332**, 527–548 (1973).
45. Barras, F. et al. The emergence of crack-like behavior of frictional rupture: edge singularity and energy balance. *Earth Planet. Sci. Lett.* **531**, 115978 (2020).
46. Yoon, C. E., Yoshimitsu, N., Ellsworth, W. L. & Beroza, G. C. Foreshocks and mainshock nucleation of the 1999 M w 7.1 Hector Mine, California, Earthquake. *J. Geophys. Res. Solid Earth* **124**, 1569–1582 (2019).
47. Chen, K. et al. Cascading and pulse-like ruptures during the 2019 Ridgecrest earthquakes in the Eastern California Shear Zone. *Nat. Commun.* **11**, 22 (2020).
48. Kilb, D., Gomberg, J. & Bodin, P. Triggering of earthquake aftershocks by dynamic stresses. *Nature* **408**, 570–574 (2000).
49. Hill, D. P. & Prejean, S. in *Treatise on Geophysics* Vol. 4 (ed. Schubert, G.) 93–110 (Elsevier, 2015).
50. Brodsky, E. E. & van der Elst, N. J. The uses of dynamic earthquake triggering. *Annu. Rev. Earth Planet. Sci.* **42**, 317–339 (2014).
51. Johnson, P. A., Savage, H., Knuth, M., Gomberg, J. & Marone, C. Effects of acoustic waves on stick–slip in granular media and implications for earthquakes. *Nature* **451**, 57–60 (2008).
52. Perfettini, H., Schmittbuhl, J. & Cochard, A. Shear and normal load perturbations on a two-dimensional continuous fault: 2. Dynamic triggering. *J. Geophys. Res. Solid Earth* **108**, 2409 (2003).
53. Lui, S. K. & Lapusta, N. Modeling high stress drops, scaling, interaction, and irregularity of repeating earthquake sequences near Parkfield. *J. Geophys. Res. Solid Earth* **123**, 10854–10879 (2018).
54. Avouac, J.-P. From geodetic imaging of seismic and aseismic fault slip to dynamic modeling of the seismic cycle. *Annu. Rev. Earth Planet. Sci.* **43**, 233–271 (2015).
55. Simons, M. et al. The 2011 magnitude 9.0 Tohoku-Oki earthquake: mosaicking the megathrust from seconds to centuries. *Science* **332**, 1421–1425 (2011).

Methods

Preparation of the rock gouge interface embedded in the polymer sample

The laboratory setup simulates earthquakes by dynamic ruptures propagating along a quartz gouge interface embedded between two plates of a polymer, Homalite-100, loaded in compression and shear (Fig. 1). Two quadrilateral plates of size 200 mm × 200 mm × 10 mm are cut out of a Homalite-100 sheet with a computer-numerical-control machine. The mating faces are then polished to a near-optical grade finish and bead-blasted with abrasive glass beads with diameter in the range 104–211 μm (refs. [36,56]). The quartz gouge interface is produced by employing a fine-ground quartz powder commercially available (MIN-U-SIL 5, US Silica), that has 99.5% content of silicon dioxide, and 96% of the grains equal to or less than 5 μm in size. A 1-mm-deep channel is milled along a portion of each mating half of the Homalite specimen (coloured in brown in Fig. 1a). The channel is 65 mm × 9 mm, with the wall thickness being 0.5 mm on each side. The channel contains the rock-gouge material during preloading and prevents it from spilling over during rupture propagation. A fine mist of glue is deposited at the bottom of each channel, and then each half of the specimen is pressed against quartz gouge, at room humidity, laid on a flat working surface. The deposit of glue allows the gouge particles to adhere to the bottom of the channel, but at the same time it does not interfere with the gouge particles through the thickness of the gouge layer. The thin layer of gouge particles glued at the bottom of each of the channels manufactured in Homalite ensures that shear failure takes place within the gouge thickness, rather than along the gouge–polymer interface. The excess gouge is subsequently removed by passing a razor blade over the interface, ensuring that the packed gouge is flush with the lateral walls of the channel. The two mating halves are then placed into contact and into the specimen holder, which in turn is positioned in the loading frame. The lateral surfaces are thoroughly cleaned to prepare them for optical imaging. Using this manufacturing protocol ensures that the shear stresses measured in the polymer are, by traction continuity, those experienced by the gouge layer and allows us to measure the frictional behaviour of rock gouge.

Controlled rupture initiation procedure

The applied load P and inclination angle α control the level of applied normal and shear prestress, $\sigma_0 = P\cos^2\alpha$ and $\tau_0 = P\sin\alpha\cos\alpha$, respectively. Two nickel-chromium (NiCr) wires (W1 and W2 in Extended Data Fig. 1) are placed across the interface at a distance of 15 mm from each other and 22.8 mm from the beginning of the imaging window. The two wires are connected to a high-voltage capacitor bank. The specimen is loaded quasi-statically to $P = 14.3$ MPa, then a dynamic rupture is initiated in Homalite by the rapid discharge of the first NiCr wire (W1 in Extended Data Fig. 1), with the capacitor set at 1.5 kV. Under these loading conditions, a supershear rupture, followed by a trailing-Rayleigh signature, is produced along a purely Homalite interface[28,37,57], and it is the only rupture the initiation of which is controlled using this experimental procedure. The other ruptures observed during the sequence are associated with the coupling between stress waves travelling in the medium and the frictional behaviour of quartz gouge. After the first sequence of dynamic events, the load is increased again to $P = 14.4$ MPa, and a new rupture is initiated from the second NiCr wire (W2 in Extended Data Fig. 1), with the capacitor set at 2.0 kV.

Full-field imaging technique

The full-field behaviour of laboratory earthquakes is captured using DIC[58] coupled with ultrahigh-speed digital photography, tailored to capture dynamic ruptures[33,36–38,59,60]. To provide a characteristic texture for image correlation, a region of interest is covered with a random speckle pattern over a white coating. The sequence of images deformed by the propagating ruptures is captured by an ultrahigh-speed camera (Shimadzu HPV-X) at one million frames per second, and is processed with image-matching algorithms to produce the evolving sequence of full-field displacements, velocities and stresses. The field of view used in this study is 47×29.4 mm^2 and is positioned entirely over the portion of the interface enriched with rock gouge, that is, it does not contain any portion of the Homalite interface. The field of view starts at the edge of the gouge closest to wires that initiate the rupture sequence and ends within the gouge layer, with 10 mm of the gouge layer being outside the field of view. Displacement fields are obtained using the commercial software VIC-2D (Correlated Solutions), with a subset size of 51×51 pixels^2 and a step size of 1 pixel, using the 'Fill-Boundary' algorithm to treat interface discontinuity. The first image in each sequence is taken as the reference configuration for the digital correlation. To denoise the displacement obtained from DIC, the fields are filtered using the nonlocal means filter[36,61,62] and are subsequently processed using the 'symmetry-adjustment' procedure[36], where the fault-parallel and fault-normal displacements are enforced to be antisymmetric and symmetric, respectively. The particle velocities and strain changes are computed from the displacements by time and space differentiation. Slip is computed by the difference of displacements at pixels immediately above and below the interface, and slip rate is its time derivative. Owing to the measurement uncertainties associated with the size of field of view used, we can resolve displacements on the order of about 0.2 μm over 1 μs (ref. [36]), and hence particle velocities of 0.2 m s^{-1}. For this reason, the smallest contour lines in the particle velocity maps are 0.25 m s^{-1}. The smallest slip rates we can resolve are on the order of 0.4 m s^{-1}. It is noted that the full-field maps of particle velocity in the Supplementary videos contain some small negative values of slip rate, which are not physical as shear stresses are oriented to cause positive slip rates. These negative slip rates are below the measurement sensitivity and hence they are due to the measurement error. Stress changes are computed from strain changes using the effective linear elastic properties of Homalite-100, with Poisson's ratio and dynamic Young's modulus $\nu = 0.35$ and $E = 5.3$ MPa, respectively[36,63]. The total stresses are obtained by adding the prestress levels τ_0 and σ_0 to the dynamic stress change[36]. The prestresses τ_0 and σ_0 are those computed using the measured P before each sequence. The stress fields obtained by numerous previous photoelastic measurements and the repeatability of the tests indicate that the assumption of uniform prestress levels is reasonable. It is noted that there may be some mild stress heterogeneities along the interface with deviations from τ_0 and σ_0, which would result in slightly different total stresses. The total shear stress given in Fig. 3c–f and obtained under the assumption of constant prestress, helps visualize the level of stress experienced by the fault, but our observations focus on the measured stress changes (Extended Data Figs. 3–6), not on the total stress levels. Friction is computed by the ratio of shear and normal stress, averaged one pixel above and below the interface[33]. Note that friction may be affected by shear stress inhomogeneities. However, here we focus on friction changes and our observations of pronounced friction variations do not depend on the assumption of constant prestress.

Theoretical estimates of the quasi-static nucleation size

The nucleation length scale on a fault governed by rate-and-state friction can be estimated using the following relation[64]:

$$h^* = \frac{1}{\pi} \frac{\mu}{(1-\nu)} \frac{b}{(b-a)^2} \frac{D_{RS}}{\sigma}$$

where μ is the shear modulus, D_{RS} is the characteristic length scale of rate and state, σ is the normal stress, and a and b are rate-and-state parameters; the relation is valid for $0.5 < a/b < 1$. This theoretical prediction provides an order of magnitude estimate, useful to design our experiments. Assuming $(b-a) = 0.005$, $b = 0.02$ and $D_{RS} = 1 \mu m$ for the rate-and-state properties of Homalite-100 (Lu 2009), computing the (quasi-static) shear modulus of Homalite from the low-strain-rate

Article

Young's modulus 2.17 GPa (ref. [63]) and Poisson's ratio $v = 0.35$, and taking $\sigma = 11$ MPa, yields a nucleation size $h^*_{\text{Homalite}} = 28.6$ mm. Nucleation sizes on the order of tens of millimetres enables us to produce dynamic ruptures within small laboratory specimens, even for relatively low confinements, which is an important advantage of this configuration. Assuming a shear modulus representative of rocks (for example, $\mu = 16$ GPa) and keeping the same rate-and-state parameters yields $h^*_{\text{rock}} = 0.57$ m. Although the actual values of the rate-and-state parameters a and b may be different for the gouge and Homalite interface, the term $b/(b-a)^2$ is likely to be of the same order of magnitude. $D_{\text{RS}} = 1\,\mu m$ is consistent with previous laboratory measurements[19,65]. Hence, employing a rock sample would result in nucleation length scales on the order of 1 m at 6 MPa of applied normal stress, consistent with the large sample size used in experimental setups using natural rocks[22,66–69]. This consideration highlights the advantage of a hybrid configuration featuring a specimen made of a polymer that results in a smaller nucleation length scale, and a layer of rock gouge embedded along the interface to explore the frictional properties more relevant to natural faults.

Rupture re-nucleation within the gouge layer and predictions for rupture speeds

The dynamically nucleated ruptures E in both rupture sequences (Fig. 2b, c) appear to propagate with supershear and even supersonic speeds (Extended Data Fig. 7f, g). These apparent rupture speeds of events E at the surface of the sample start with values much larger than the wave speeds and then monotonically decrease with propagation along the interface (Extended Data Fig. 7). The apparent rupture speeds are measured along the lateral free surface on which the displacements are calculated, using the contour lines of the slip rate in the x_1–t plane, where t is time. To identify the rupture fronts, we consider contour lines of 0.75 m s^{-1} and 1.5 m s^{-1} of slip rate as thresholds (for sequences 1 and 2, respectively, Extended Data Fig. 7b, c).

These unphysically large rupture speeds can be explained by rupture initiating within the thickness of the gouge layer and dynamically propagating towards the surface of observation with the actual rupture speed V_{act} (Extended Data Fig. 7a). Indeed, the acceleration on the lateral surface (during events E from both sequences) takes place over less than 5–10 mm, the length smaller than the 10-mm thickness of the interface, indicating that the thickness cannot be ignored. In the simplest case of the rupture starting from a mid-point of the interface and spreading with a constant (actual) rupture speed V_{act}, the apparent rupture speed V_{app} observed on the lateral free surface is given by the following relation:

$$V_{\text{app}} = \frac{AB}{\Delta t} = V_{\text{act}}\sqrt{1 + \frac{2t_0}{\Delta t}}$$

where t_0 is the time at which the rupture front reaches the free surface at the location where measurements are performed, denoted by point A in Extended Data Fig. 7a and corresponding to the position x_0 along the x_1 axis, on the free surface. The time interval $\Delta t = t - t_0$ is the time it takes the rupture front to advance from A to B along the free surface. The location of point B along x_1 is given by:

$$x_1 = x_0 + \int_0^{\Delta t} V_{\text{act}}\sqrt{1 + \frac{2t_0}{\Delta t'}}\,d(\Delta t')$$

We fit this analytical model to the experimentally measured propagation of the rupture front along the free surface of the dynamically nucleated ruptures. We assume a constant V_{act} and assume initiation from a point such that $t_0 = (h/2)/V_{\text{act}}$.

The fit of the analytical model to the experimental measurements estimates actual rupture speeds of $V^I_{\text{act}} = 0.26$ km s^{-1} and $V^{II}_{\text{act}} = 0.46$ km s^{-1}, for ruptures E of sequences 1 and 2, respectively, and

$t_0 = 23.6\,\mu s$ and $t_0 = 10.8\,\mu s$ (Extended Data Fig. 7d, e). It is noted that both of these rupture speeds are subshear. In fact, considering the high-strain-rate shear-wave speed of Homalite-100 ($c_s = 1.29$ km s^{-1}), $V^I_{\text{act}} = 0.26$ km s$^{-1} = 0.16\,c_s$, and $V^{II}_{\text{act}} = 0.46$ km s$^{-1} = 0.36\,c_s$.

Hence the observed apparent, variable speed V_{app} of the intersection of the rupture front and the observational surface can be well matched for V_{act} of $0.16\,c_s$ and $0.36\,c_s$, for ruptures E in each of the two sequences, respectively, quite reasonable initial rupture speed of just-initiated events (Extended Data Fig. 7, Methods). Of course, the actual rupture probably starts from a finite-size nucleation region and continuously accelerates during the initial propagation, making V_{act} an estimate of the average rupture speed over the initial roughly 6–8 mm of propagation.

Interpreting friction strengthening through standard rate-and-state friction formulations

In rate-and-state friction formulations, friction is a function of slip velocity $\dot{\delta} = V$ and of a state variable θ, describing the evolution of the contacting asperities[4,6,70–74]:

$$f = f_* + a\log\left(\frac{V}{V_*}\right) + b\log\left(\frac{V_*\theta}{L}\right)$$

where f_* is the reference friction coefficient at the reference slip rate V_*, a and b are rate-and-state parameters, and L is the characteristic slip for the evolution of the state variable. One form for the evolution law of the state variable is the so-called aging law[70–72] and is widely used in the literature:

$$\frac{d\theta}{dt} = 1 - \frac{V\theta}{L}$$

Several other evolution laws have been proposed, including the slip law[72] and the composite law[75,76]. According to rate-and-state laws, during changes of slip velocity, friction has history-dependent effects, which are described by the state variable. At constant slip rate and once enough slip has occurred, it becomes solely rate dependent. At steady state, the friction coefficient takes the form:

$$f_{\text{ss}} = f_* + (a - b)\log\left(\frac{V}{V_*}\right)$$

Depending on whether $(a - b)$ is positive or negative, friction can increase or decrease with increasing slip velocity and be velocity strengthening or velocity weakening. One important feature of rate-and-state friction is that when slip velocity increases rapidly from V_1 to V_2, with negligible slip so that the state variable cannot evolve, the friction change is given by $\Delta f = a\log V_2/V_1$, the so-called direct effect (which also occurs with negligible slip). It is noted that regardless of whether friction is velocity strengthening or velocity weakening, the direct effect always results in an immediate friction increase upon an increase in slip velocity, as a is a positive quantity. If slip velocity increases gradually from V_1 to V_2, with ample slip so that the state variable can evolve to its steady state, the friction change is given by $\Delta f = (a - b)\log V_2/V_1$. According to laboratory measurements, both a and $(a - b)$ are of the order of, and typically less than, 0.01 for rock surfaces and gouges[4,6]. It is noted that if the strengthening in our experiments were due to the direct effect of otherwise rate-weakening rate-and-state friction, then the strengthening would occur over negligible slips compared with the weakening.

Data availability

The data generated in this study are available through the CaltechDATA repository at https://data.caltech.edu/records/2155. Source data are provided with this paper.

56. Mello, M., Bhat, H. S., Rosakis, A. J. & Kanamori, H. Identifying the unique ground motion signatures of supershear earthquakes: theory and experiments. *Tectonophysics* **493**, 297–326 (2010).

57. Lu, X., Rosakis, A. J. & Lapusta, N. Rupture modes in laboratory earthquakes: effect of fault prestress and nucleation conditions. *J. Geophys. Res. Solid Earth* **115**, B12302 (2010).

58. Sutton, M. A., Orteu, J. J. & Schreier, H. *Image Correlation for Shape, Motion and Deformation Measurements: Basic Concepts, Theory and Applications* (Springer, 2009).

59. Tal, Y., Rubino, V., Rosakis, A. J. & Lapusta, N. Enhanced digital image correlation analysis of ruptures with enforced traction continuity conditions across interfaces. *Appl. Sci.* **9**, 1625 (2019).

60. Rosakis, A., Rubino, V. & Lapusta, N. Recent milestones in unraveling the full-field structure of dynamic shear cracks and fault ruptures in real-time: from photoelasticity to ultrahigh-speed digital image correlation. *J. Appl. Mech.* **87**, 030801 (2020).

61. Buades, A., Coll, B. & Morel, J. M. Nonlocal image and movie denoising. *Int. J. Comput. Vis.* **76**, 123–139 (2008).

62. Rubino, V., Lapusta, N., Rosakis, A. J., Leprince, S. & Avouac, J. P. Static laboratory earthquake measurements with the digital image correlation method. *Exp. Mech.* **55**, 77–94 (2015).

63. Singh, R. P. & Parameswaran, V. An experimental investigation of dynamic crack propagation in a brittle material reinforced with a ductile layer. *Opt. Lasers Eng.* **40**, 289–306 (2003).

64. Rubin, A. M. & Ampuero, J. P. Earthquake nucleation on (aging) rate and state faults. *J. Geophys. Res. Solid Earth* **110**, B11312 (2005).

65. Marone, C. & Kilgore, B. Scaling of the critical slip distance for seismic faulting with shear strain in fault zones. *Nature* **362**, 618–621 (1993).

66. Dieterich, J. H. Potential for geophysical experiments in large scale tests. *Geophys. Res. Lett.* **8**, 653–656 (1981).

67. Okubo, P. G. & Dieterich, J. H. Effects of physical fault properties on frictional instabilities produced on simulated faults. *J. Geophys. Res. Solid Earth* **89**, 5817–5827 (1984).

68. Beeler, N. et al. Observed source parameters for dynamic rupture with non-uniform initial stress and relatively high fracture energy. *J. Struct. Geol.* **38**, 77–89 (2012).

69. McLaskey, G. C. Earthquake initiation from laboratory observations and implications for foreshocks. *J. Geophys. Res. Solid Earth* **124**, 12882–12904 (2019).

70. Dieterich, J. H. Modeling of rock friction: 1. Experimental results and constitutive equations. *J. Geophys. Res. Solid Earth* **84**, 2161–2168 (1979).

71. Dieterich, J. H. in *Mechanical Behavior of Crustal Rocks: The Handin Volume* (eds Carter, N. L., Friedman, M., Logan, J. M. & Stearns, D. W.) 103–120 (AGU, Washington DC, 1981).

72. Ruina, A. Slip instability and state variable friction laws. *J. Geophys. Res. Solid Earth* **88**, 10359–10370 (1983).

73. Blanpied, M., Lockner, D. & Byerlee, J. Fault stability inferred from granite sliding experiments at hydrothermal conditions. *Geophys. Res. Lett.* **18**, 609–612 (1991).

74. Blanpied, M. L., Lockner, D. A. & Byerlee, J. D. Frictional slip of granite at hydrothermal conditions. *J. Geophys. Res. Solid Earth* **100**, 13045–13064 (1995).

75. Kato, N. & Tullis, T. E. A composite rate-and state-dependent law for rock friction. *Geophys. Res. Lett.* **28**, 1103–1106 (2001).

76. Kato, N. & Tullis, T. E. Numerical simulation of seismic cycles with a composite rate-and state-dependent friction law. *Bull. Seismol. Soc. Am.* **93**, 841–853 (2003).

Author contributions V.R., A.J.R. and N.L. contributed to developing the main ideas, interpreting the results and producing the manuscript. V.R. performed the measurements and analysed the data.

Loading time history

$\tau_0 = 6.1$ MPa
$\sigma_0 = 11.0$ MPa

$P = 14.3$ MPa

$P = 14.4$ MPa

Ruptures sequence #1

Ruptures sequence #2

10 mm

P

Rock gouge layer

Multiple initiation sites

47 mm

200 mm

15 22.8 mm mm

α

Field of view

W1 W2

NiCr wires

P

Quartz gouge layer

47 mm

Lower half of the field of view
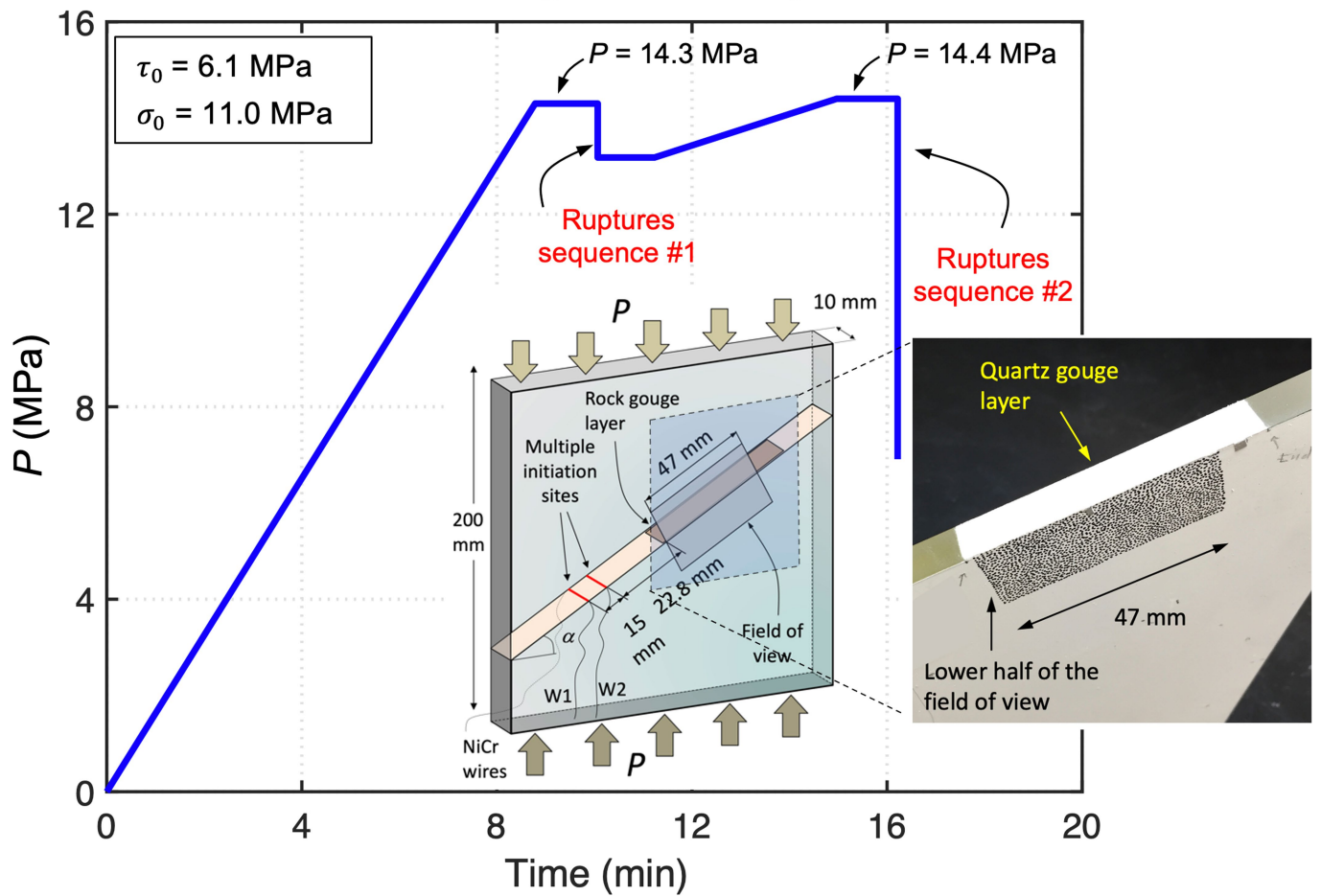
Extended Data Fig. 1 | Specimen loading time history. The specimen is compressed in the axial direction by a load P, which results in a resolved normal and shear stresses on the interface inclined at an angle α, given by $\sigma_0 = P\cos^2\alpha$ and $\tau_0 = P\sin\alpha\cos\alpha$, respectively. The load is quasi-statically increased up to $P = 14.3$ MPa, then the first sequence of ruptures is triggered by the discharge of wire W1. After the first sequence of recorded events, and additional slip occurring after the end of recording, the load drops to $P = 13.3$ MPa. The far-field loading is subsequently increased to $P = 14.4$ MPa and the second sequence of events is triggered by the discharge of W2. The inset to the right shows the bottom half of the sample with the gouge insert and the location of the lower half of the field of view with the speckle pattern used to analyse the sequence of images with the digital image correlation method.
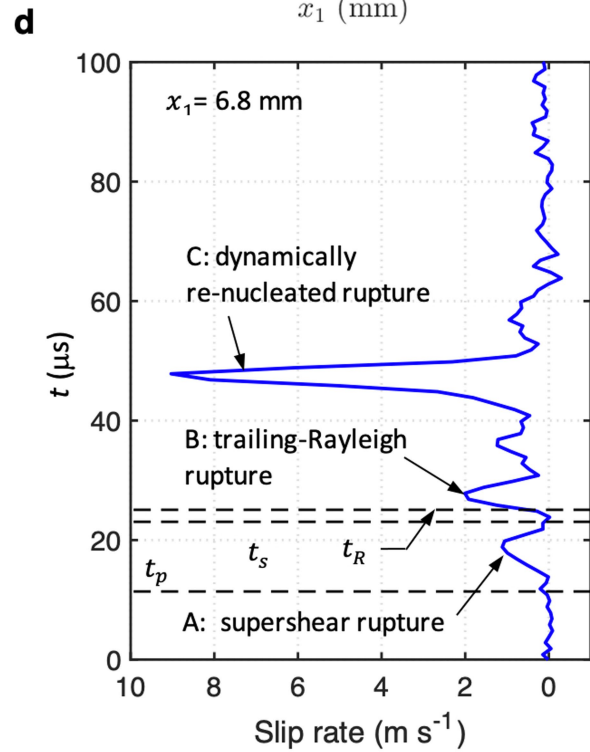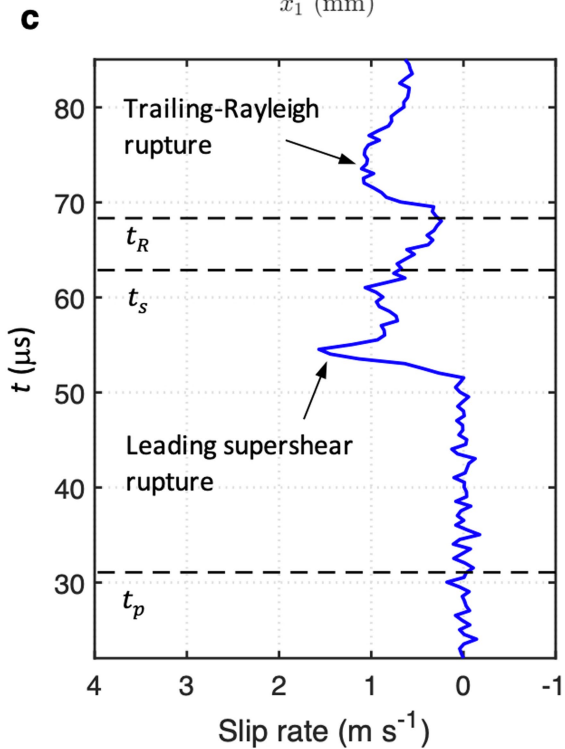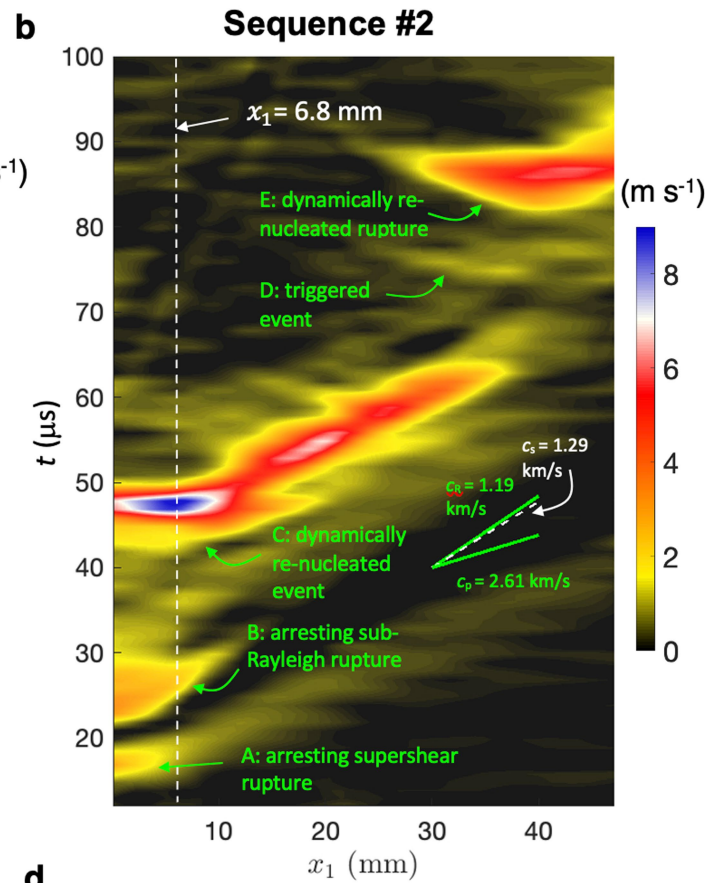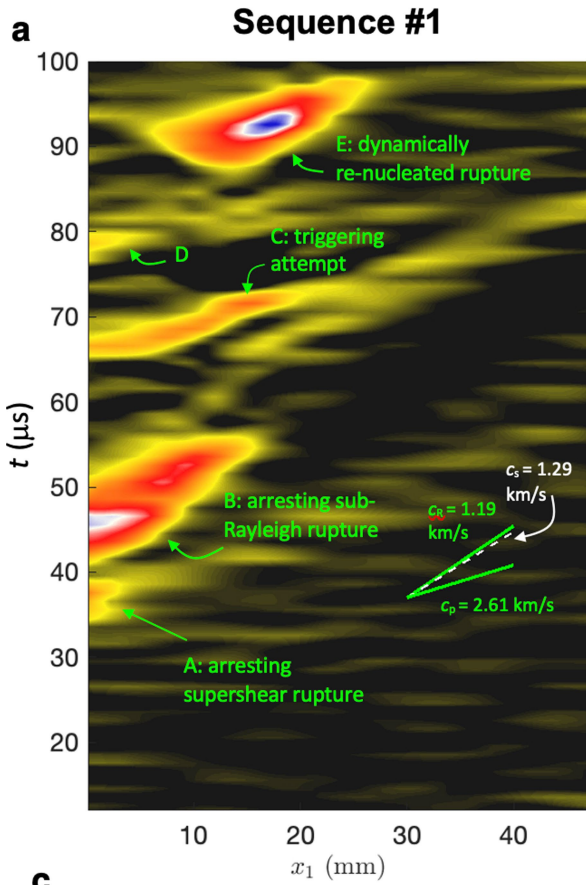
Extended Data Fig. 2 | Slip-velocity time history. a, b, Slip-velocity maps as in Fig. 1b,c plotted over the same time and space range but using a different slip-velocity scale of 4 m s⁻¹ and 9 m s⁻¹, respectively. **c,** Slip-velocity time history for a reference rupture propagating in a Homalite interface, displaying a supershear rupture followed by a trailing-Rayleigh signature (data from ref. [37]). **d,** Slip-velocity time history for the second rupture sequence at the location $x_1 = 6.9$ mm, shown by a dashed white line in **b**.

Sequence #1 – part 1

Fault-parallel velocity

Shear stress change
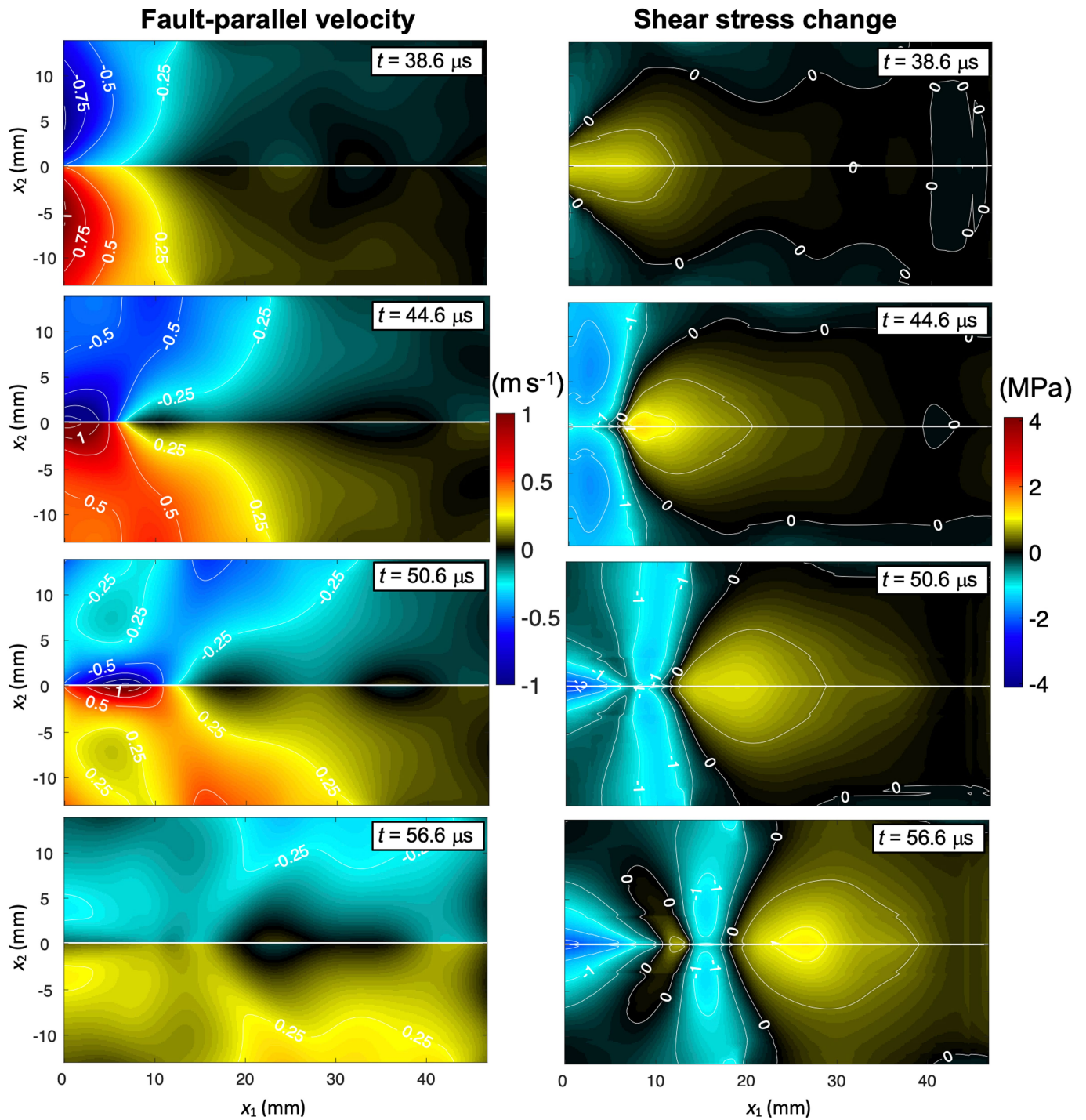
Extended Data Fig. 3 | Snapshots of the full-field distributions of fault-parallel particle velocity and shear stress change during the initial phase of the first rupture sequence. The full-field maps show, top to bottom, the supershear rupture arrest (event A) at $t = 38.6$ μs, the arrival of the sub-Rayleigh rupture (event B) at $t = 44.6$ μs, its propagation ($t = 50.6$ μs), and subsequent arrest ($t = 56.6$ μs). Note that the stress concentration at the arrest time of event B is relatively minor and at a different location from where event E is dynamically re-nucleated later (Extended Data Fig. 4).

Extended Data Fig. 4 | Snapshots of the full-field distributions of fault-parallel particle velocity and shear stress change during the later phase of the first rupture sequence. The full-field maps of the propagation of a triggering attempt (event D) at t = 72.6 µs (top row) indicate that, even at this intermediate time between the arrest of event B at 56.6 µs (Extended Data Fig. 3) and dynamic initiation of event E at t = 87.6 µs (second row), the largest stress concentration is not where event E initiates, highlighting the dynamic and transient nature of shear stress changes that balance the evolving frictional resistance. The third and bottom rows illustrate the subsequent propagation of event E (t = 88.6 µs and 92.6 µs).
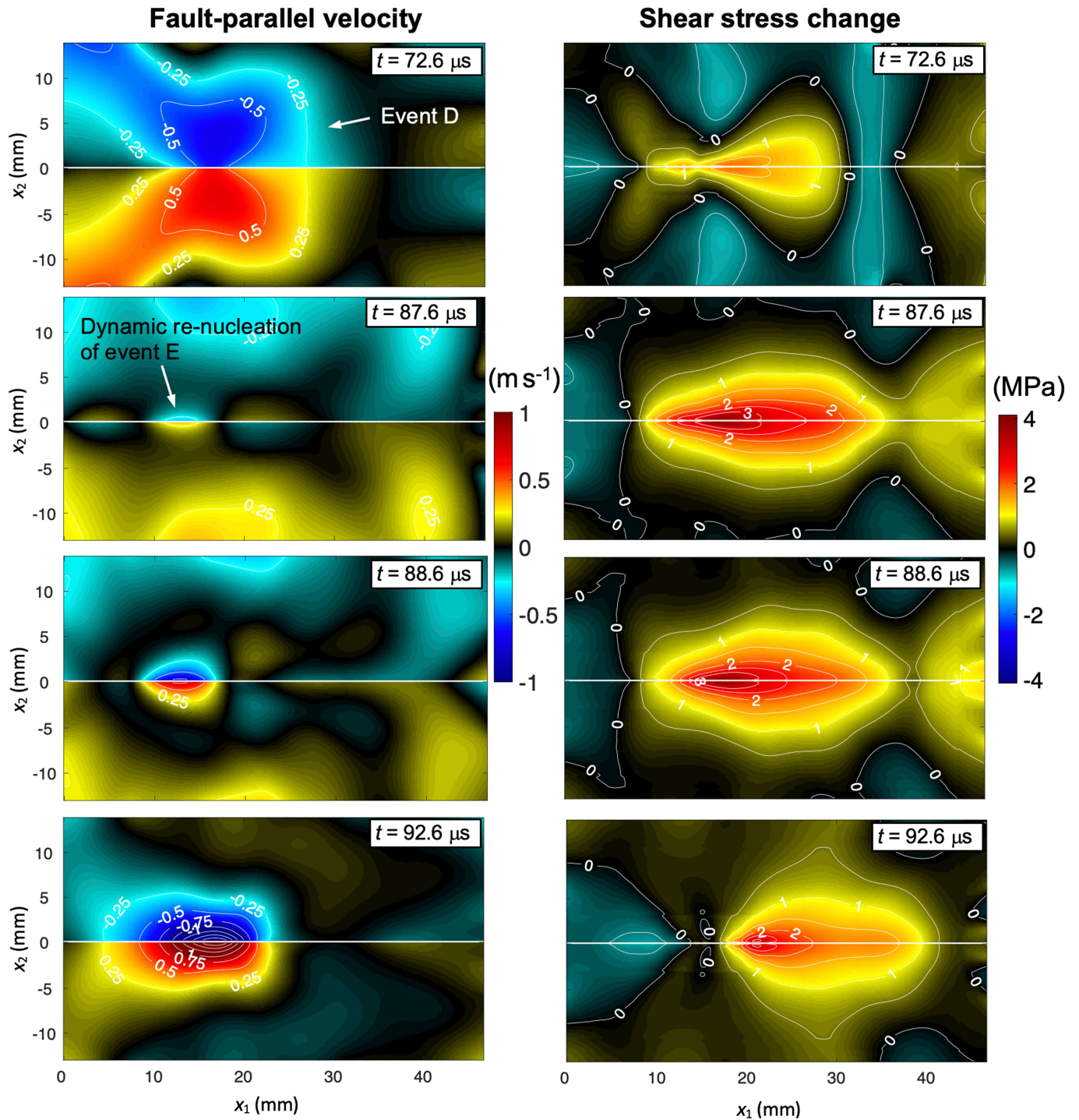
Sequence #2 – part 1
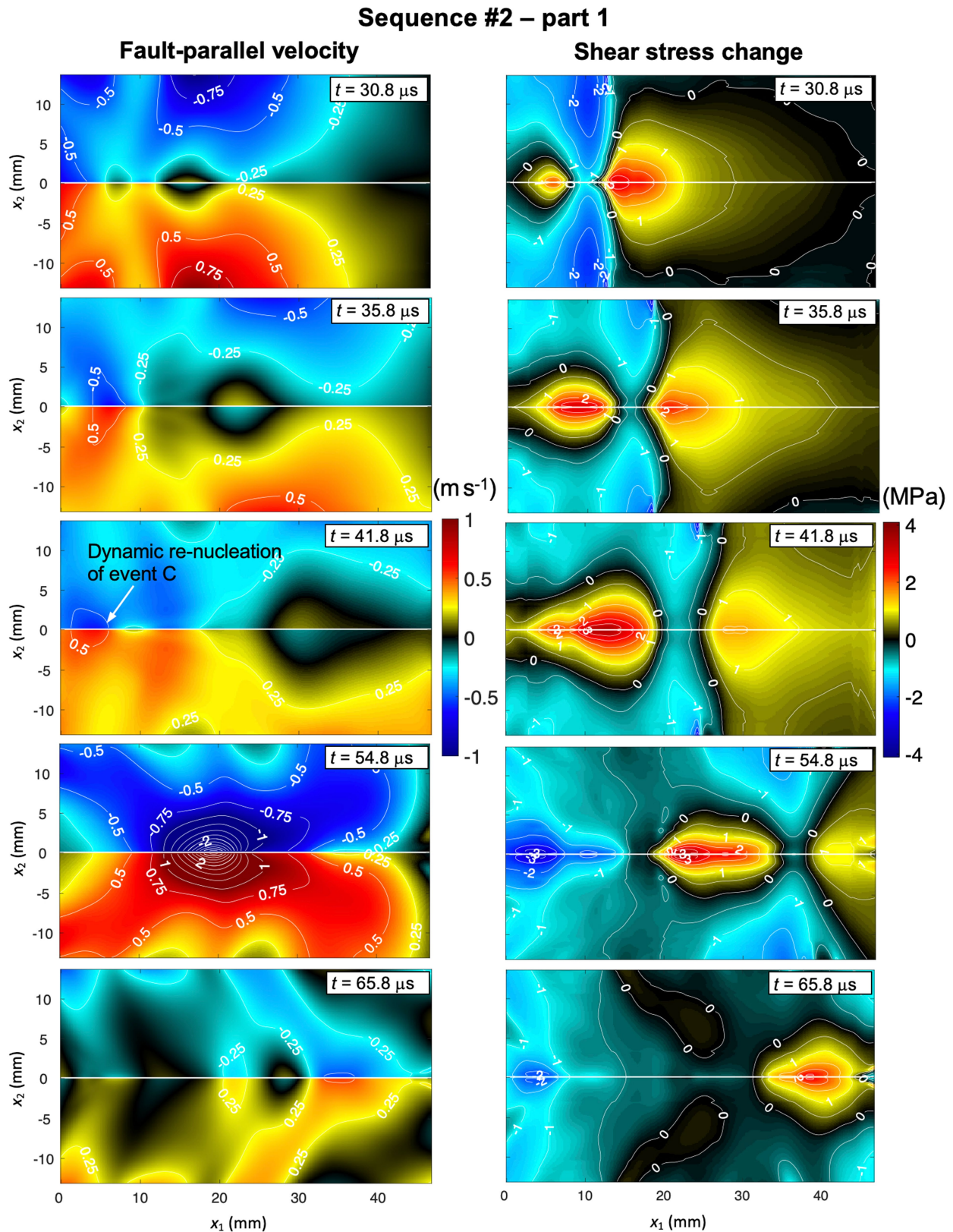
Extended Data Fig. 5 | Snapshots of the full-field distributions of fault-parallel particle velocity and shear stress change during the early phase of the second rupture sequence. The full-field maps show the arrest of the sub-Rayleigh rupture (event B) at $t = 30.8\ \mu s$; slower slip occurring at the edge at $t = 35.8\ \mu s$, with the corresponding increasing shear stress illustrating how strengthening occurs; nucleation of event C at $t = 41.8\ \mu s$; and its progression ($t = 54.8\ \mu s$ and $t = 65.8\ \mu s$).

Sequence #2 – part 2
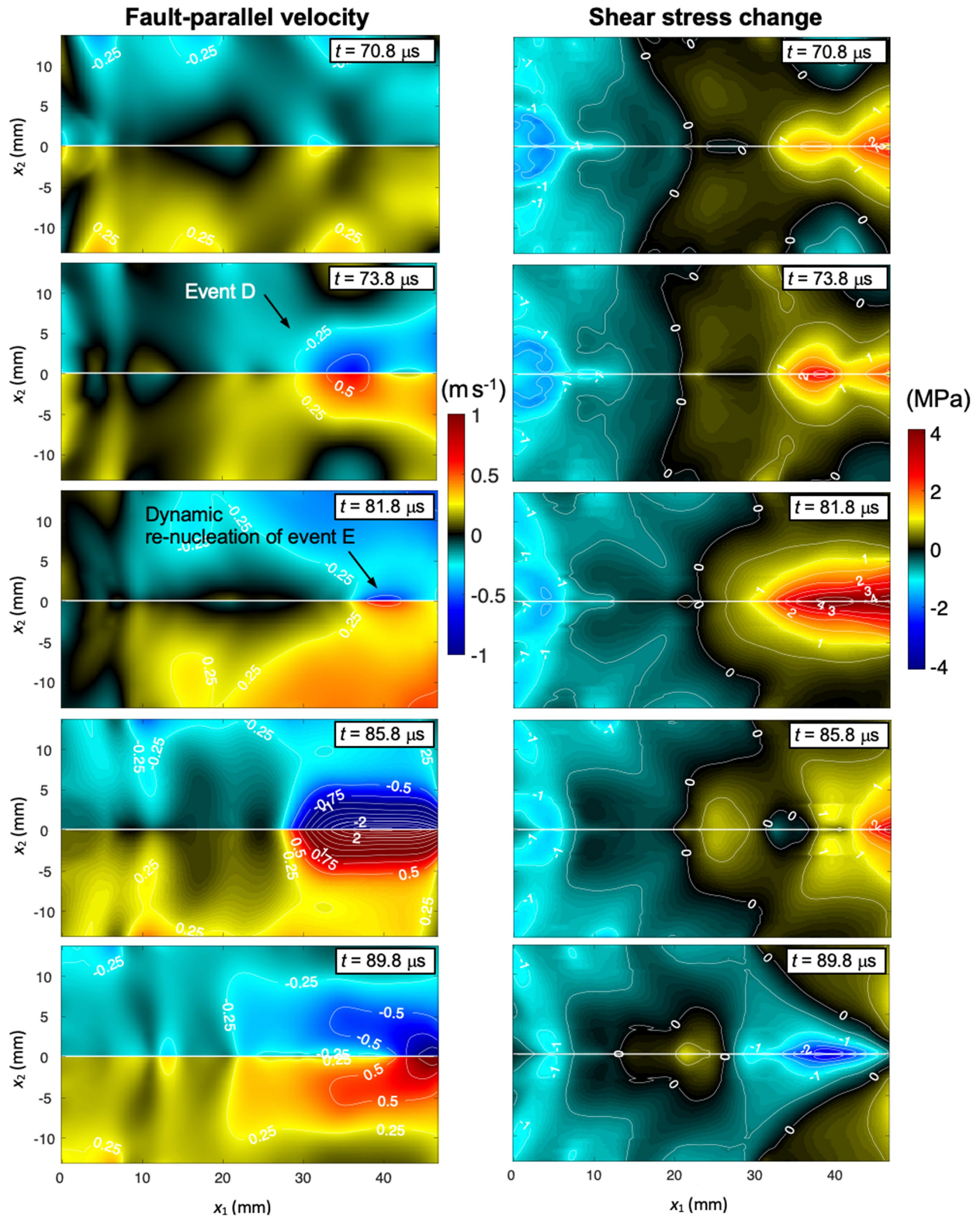
Extended Data Fig. 6 | Snapshots of the full-field distributions of fault-parallel particle velocity and shear stress change during the later phase of the second rupture sequence. The full-field maps show the fields right after the arrest of event C ($t = 72.6\,\mu s$), featuring a relatively mild stress concentration where event E is eventually triggered; a triggering attempt (event D) at $t = 73.6\,\mu s$; dynamic nucleation of event E at $t = 81.8\,\mu s$, with substantial dynamic increase in shear stress since event D; and subsequent propagation of event E at $t = 85.8\,\mu s$ and $89.8\,\mu s$. The rupture initially propagates bilaterally ($t = 83.8 – 87.8\,\mu s$), with the left front eventually losing steam, and the right front exiting the field of view as a strong rupture. This rupture results in a pronounced shear stress drop of $\Delta\tau = 7.5\,MPa$ ($t = 83.8 – 89.8\,\mu s$).
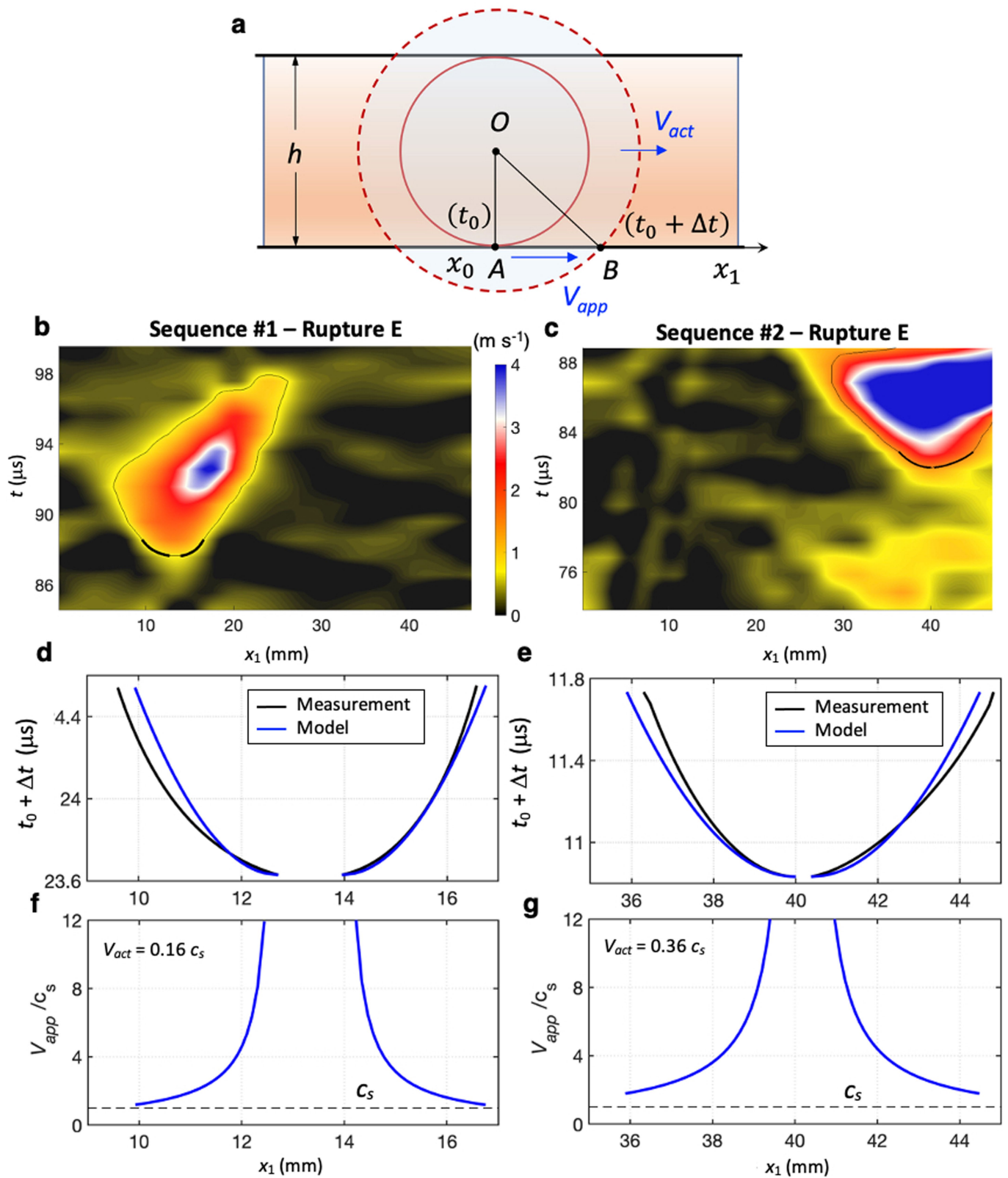
Extended Data Fig. 7 | Model showing the actual and apparent rupture speeds. a, Schematics showing a dynamic rupture originating within the gouge layer at O and reaching the surface of observation at the location A at time t_0, while propagating at a rupture speed V_{act}. As the rupture front swipes through the free surface, where measurements are performed, it results in an apparent rupture speed V_{app}. **b, c**, Maps of slip-velocity histories for ruptures E, with black lines outlining the position of the rupture front. **d, e**, Contour lines of the rupture fronts (black lines), the same as in **b, c**, and the fit using the analytical model (blue lines) described in the text. **f, g**, The apparent rupture speed on the free surface, for events E in sequences 1 and 2, respectively, showing unphysical initially supersonic rupture speeds. Using the model in **a**, these unphysical apparent rupture speeds can be explained by the actual rupture speeds of $0.16\,c_s$ and $0.36\,c_s$, respectively.
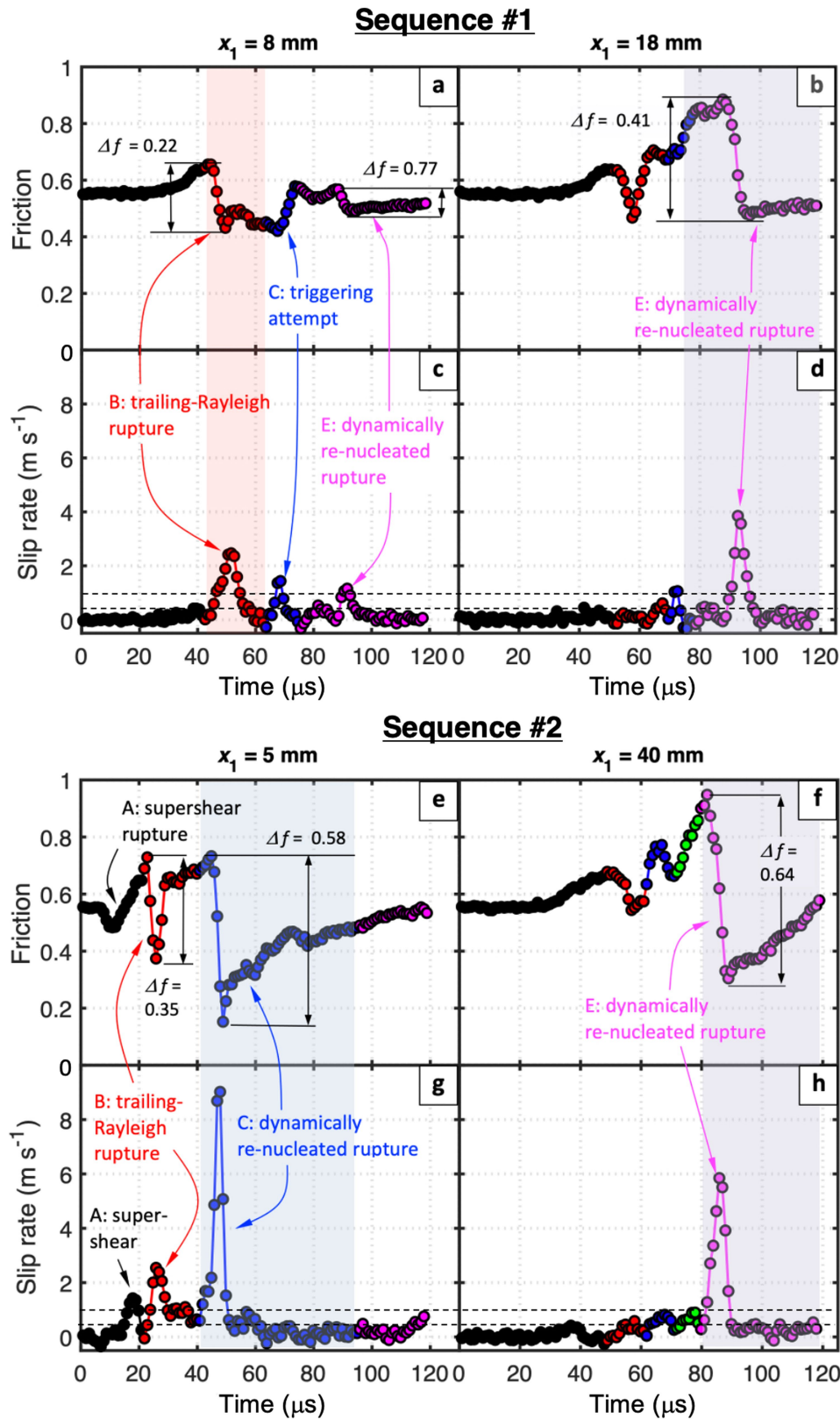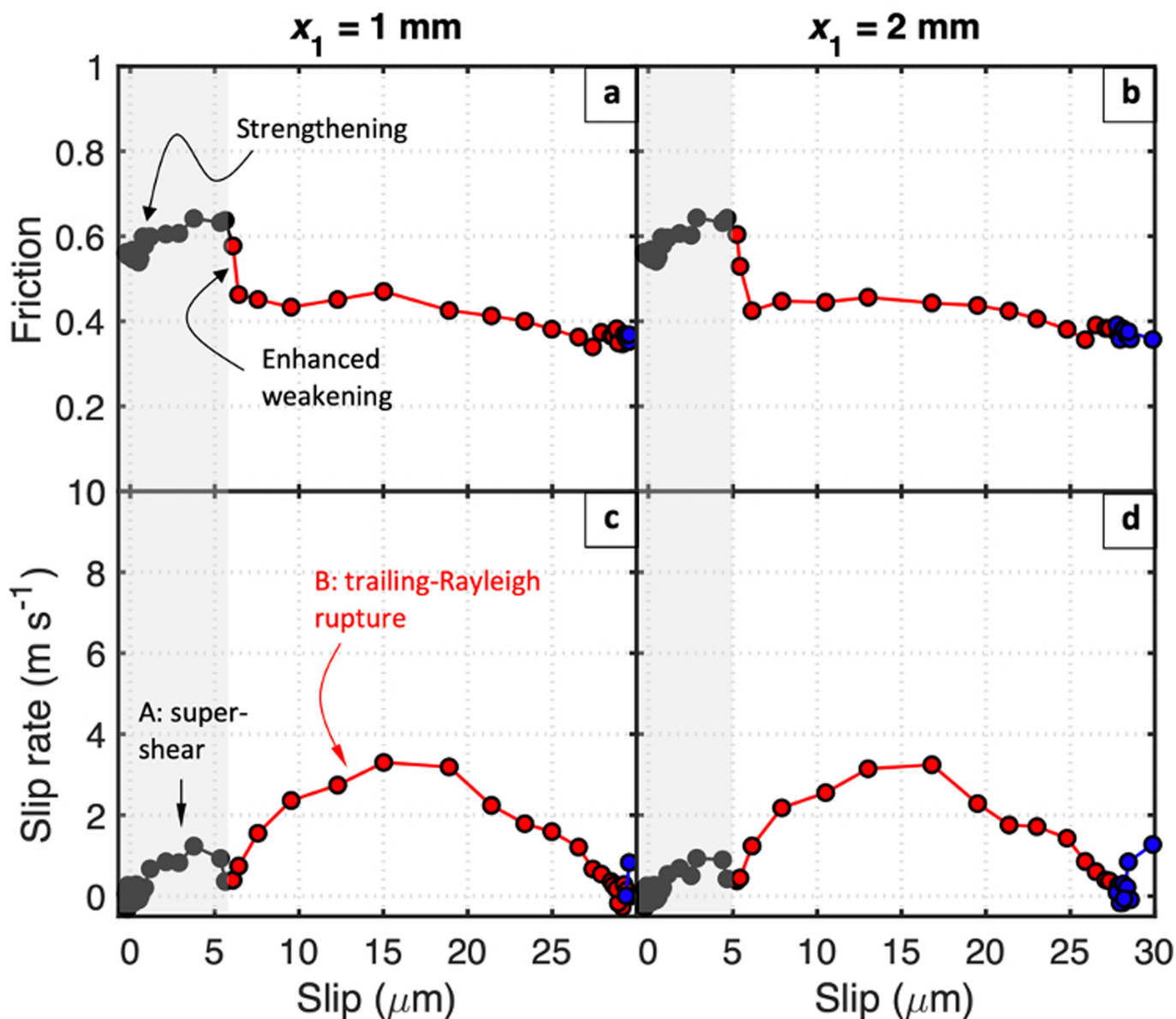
Extended Data Fig. 8 | Friction and slip-velocity time histories within the rock gouge with pronounced and repeated strengthening, enhanced weakening, and healing. Friction versus time (**a**, **b**, **e**, **f**) and slip rate versus time (**c**, **d**, **g**, **h**) or the two rupture sequences, for selected locations along the interface. As in Fig. 4, but with friction and slip rate plotted versus time rather than versus slip. Colours are the same as in Fig. 2. Similarly to the friction evolution with slip (Fig. 4), the friction time histories shown here are characterized by marked strengthening, for slip rates as high as 0.5–2 m s^{-1}, followed by dramatic weakening at higher slip rates consistent with flash heating. In both sequences, the first supershear ruptures are arrested, with velocity-strengthening behaviour, whereas the trailing-Rayleigh ruptures and subsequent dynamic events result in substantial velocity weakening. The plots of friction versus time emphasize the strengthening, which is more compressed in the plots versus slip. The slip-rate time histories show how rapidly the slip rate changes.
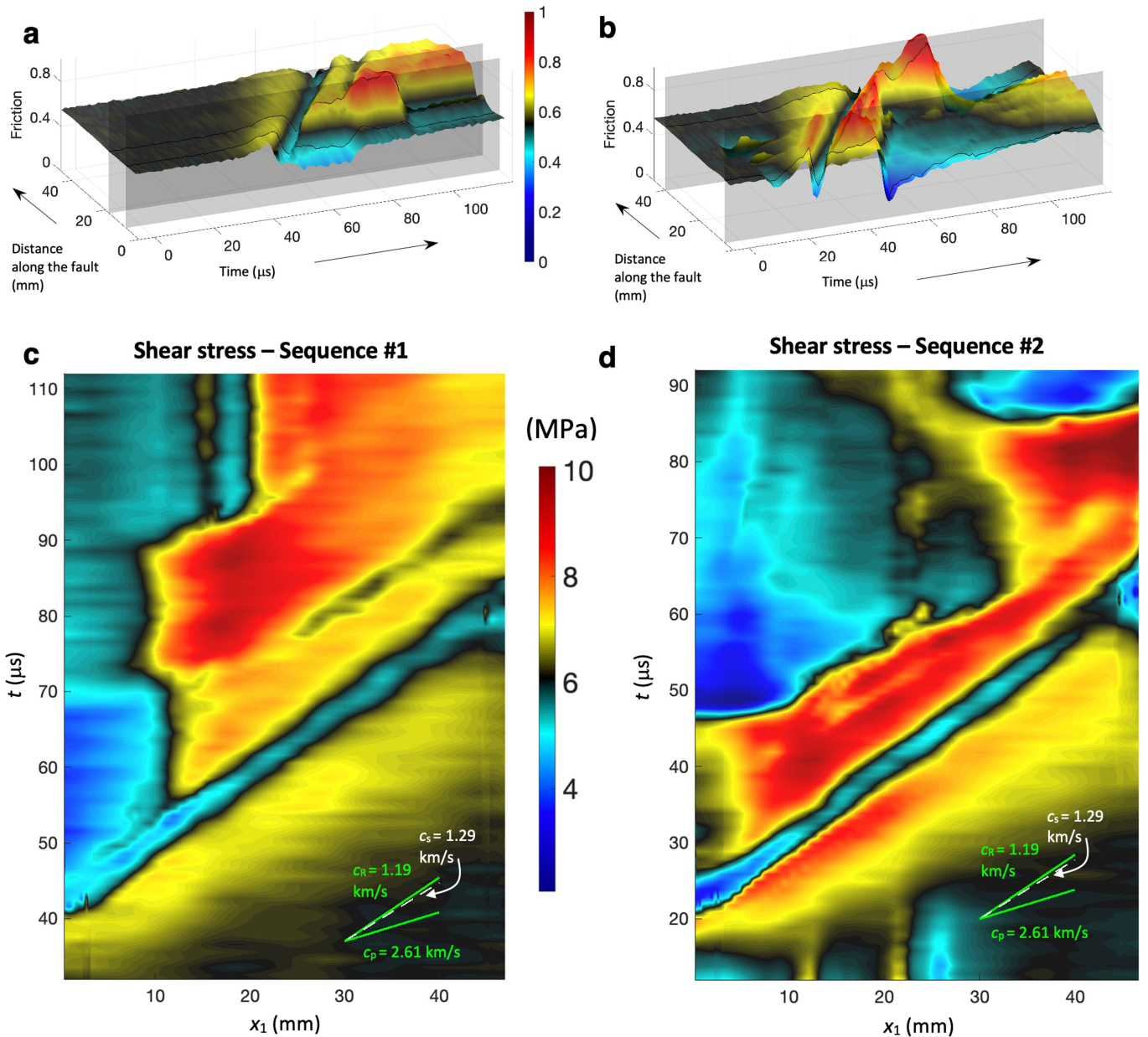
Extended Data Fig. 9 | Friction and shear stress time histories along the interface for the two sequences of laboratory earthquakes. a, **b**, First (**a**) and second (**b**) sequence of ruptures (same as in Fig. 1e). This figure presents the two cases next to each other for comparison. The friction coefficient before ruptures arrival, $f_0 = \tau_0/\sigma_0 = 0.55$, is represented in black, while the red regions indicate the friction coefficient increase associated with strengthening and the blue regions corresponding to the pronounced weakening, consistent with flash heating. Planes intersecting the friction surface are shown at the two locations analysed in Fig. 4 and Extended Data Fig. 8. The planes are at $x_1 = 8$ mm and $x_1 = 18$ mm, and at $x_1 = 5$ mm and $x_1 = 40$ mm, for the first and second sequences, respectively. **c**, **d**, Maps of the shear stress for the first and second sequence, respectively, showing the highly variable and transient nature of the

stress field. The shear stress increase (yellow-to-red) and then decrease (blue) traversing the entire field of view (from approximately 35 to approximately 80 and approximately 20 to approximately 60 microseconds for the first and second sequence, respectively) are associated with slip in events B and then correspond to the continued propagation of the pressure and shear waves that increase stress as well as Rayleigh waves that decrease stress associated with the prior slip of (now arrested) rupture B; note that the (dynamic) shear stress decrease is not associated with any slip occurring on the interface. Arrest of slip events leads to stress concentrations which, together with dynamic stress waves from ongoing slip on the Homalite interface as well as intermitted slip in the gouge, and dynamic weakening, promote dynamic nucleation of subsequent slip events.

Extended Data Fig. 10 | Additional evidence for velocity strengthening in quartz gouge. Friction versus slip (**a**, **b**) and slip rate versus slip (**c**, **d**) for rupture sequence 1 at the edge of the gouge layer, $x_1 = 1$ mm and $x_2 = 2$ mm. These plots show that friction increases during event A over slips of roughly 5 μm, while the slip velocity increases from roughly 0.5 m s^{-1} to a peak value of over 1 m s^{-1}. In event B (red), substantial weakening of ~0.15 in friction coefficient occurs over slip scales of just 2 μm or so as slip rate increases. At $x_1 = 8$ mm (Fig. 4a), weakening of 0.22 occurs over slip scales of approximately 5 μm, again indicating that weakening of 0.1 in friction occurs over slips of 2–3 μm. Hence the strengthening and weakening occur over similar slip scales indicating that both are sustained friction response. Note that if the strengthening were due to the direct effect of otherwise rate-weakening rate-and-state friction, then the strengthening would occur over negligible slips compared to the weakening.